



**TOR VERGATA**  
UNIVERSITÀ DEGLI STUDI DI ROMA

DOTTORATO DI RICERCA IN FISICA

CICLO DEL CORSO DI DOTTORATO XXXIII

**Search for the FCNC decay of top-quark in  
c-quark and Z boson using the ATLAS detector**

**LORENZO MARCOCCIA**

**A.A. 2020/2021**

**DOCENTE GUIDA: Prof. LUCIO CERRITO**

**COORDINATORE: Prof. ROBERTO BENZI**

A dissertation submitted to the University of Rome Tor Vergata in accordance with the requirements of the degree of DOCTOR OF PHILOSOPHY in the Faculty of Physics.

**32 NOVEMBER 2184**

*'The wrong view of science  
betrays itself in the craving to be right;  
for it is not his possession of knowledge,  
of irrefutable truth, that makes the man of science,  
but his persistent and recklessly critical quest for truth.'*

(Karl Popper, The Logic of Scientific Discovery)

---

## Ringraziamenti

---

Merci, merci, merci.



---

## Abstract

---

Blablabla.



---

# Contents

---

<b>Introduction</b>	<b>1</b>
<b>1 The theory framework</b>	<b>3</b>
1.1 The gauge principle in quantum field theory . . . . .	4
1.1.1 Quantum Chromodynamics . . . . .	5
1.1.2 The electro-weak sector . . . . .	6
1.1.2.1 GIM mechanism . . . . .	8
1.1.2.2 CKM matrix . . . . .	9
1.2 Top quark physics . . . . .	10
1.2.1 Production . . . . .	10
1.2.2 Decay channels . . . . .	11
1.3 Theories for physics beyond the Standard Model . . . . .	12
1.3.1 Quark singlets . . . . .	14
1.3.2 Two Higgs Doublet Model . . . . .	15
1.3.3 Minimal Supersymmetric Standard Model . . . . .	16
<b>2 The LHC accelerator and the ATLAS experiment</b>	<b>18</b>
2.1 The LHC accelerator . . . . .	19
2.2 The ATLAS detector . . . . .	22
2.2.1 Magnet system . . . . .	24
2.2.2 The inner Detector . . . . .	24
2.2.3 The Calorimetric System . . . . .	25
2.2.4 Muon spectrometer . . . . .	27
2.2.5 ATLAS trigger and data acquisition . . . . .	29

<b>3</b>	<b>The Trigger system upgrade for High-Luminosity LHC</b>	<b>30</b>
3.1	ATLAS Barrel Muon Trigger . . . . .	31
3.2	BI upgrade for Phase II . . . . .	34
3.2.1	RPC upgrade . . . . .	37
3.2.2	Trigger scheme . . . . .	39
3.3	Hit digitization in the BI region . . . . .	40
3.3.1	The cluster size model . . . . .	41
3.3.2	Timing . . . . .	46
3.3.3	BI RPCs with two-sides $\eta - \eta$ readout . . . . .	48
3.4	L0 barrel trigger efficiency . . . . .	48
3.4.0.1	BM and BO retrofitting . . . . .	49
3.4.0.2	Dropping BIR and BIM chambers . . . . .	49
<b>4</b>	<b>The Soft Muon Tagging</b>	<b>54</b>
4.1	The soft muons . . . . .	55
4.2	Working Point definition . . . . .	56
4.3	Mistag rate measurement . . . . .	57
4.4	Efficiency measurements . . . . .	58
<b>5</b>	<b>Search for the FCNC decay of top-quark in c-quark and Z boson</b>	<b>59</b>
5.1	Physics motivation . . . . .	60
5.2	Analysis strategy . . . . .	61
5.3	MC simulated samples . . . . .	62
5.4	Event selections and reconstruction . . . . .	63
5.4.1	Offline selection . . . . .	64
5.4.2	Event classification . . . . .	65
5.4.3	Background control and validation regions . . . . .	66
5.5	Estimation of the fake-lepton background . . . . .	67
5.5.1	Fake Scale Factors fit regions . . . . .	68
5.5.2	Determination of Fake Scale Factors . . . . .	68
5.6	Signal-to-background discrimination . . . . .	69
5.7	Background estimation . . . . .	70
5.7.1	Signal injection tests . . . . .	71
5.8	Systematic uncertainties . . . . .	72
5.9	Statistical analysis . . . . .	73
5.10	Results . . . . .	74
<b>6</b>	<b>Conclusions</b>	<b>75</b>
<b>A</b>	<b>Mass Resolution</b>	<b>76</b>
<b>References</b>		<b>77</b>

---

## Introduction

---

## CONTENTS

# CHAPTER 1

---

## The theory framework

---

The construction of the Standard Model is the result of a long series of experiments and brilliant ideas in both theoretical and experimental fields. Towards the end of the 1960s, knowledge of what we consider to be the constituents elements of nature and the fundamental interactions among them, it was organized in the so-called Standard Model (MS), which aims to be a "theory of everything".

More recently, the only missing piece towards the completion of the SM, the Higgs boson, was discovered by the ATLAS and CMS collaborations.

The ambition is to find a theoretical representation of all phenomena experimentally accessible.

Since particle physics is characterized by phenomena that are both relativistic than quantum, the description of the Standard Model relies on the formalism of *Quantum Field Theories* (QFT), synthesis of quantum mechanical theory and relativistic. In these terms, the concept of field is associated both to material particles and to forces. Particles are mere manifestations of field: they are identified with the quanta of the material fields and force fields and the interaction among particles is determined by the exchange of virtual quanta of the field.

To search for extensions of the SM is possible postulate a scale of new physics high enough such that it will manifest itself through deviations of known observable, usually at high energies.

In this chapter, a concise description of the SM will be presented, from the gauge principle to the description of several theories for physics beyond the Standard Model which are crucial for the search of FCNC decay of top quark.

## 1.1 The gauge principle in quantum field theory

The mathematical framework of the SM is based on a quantum field theory description of the particles and their interactions. The interaction is a consequence of the invariance of physics under certain general symmetries: these invariances are called *gauge* because there is freedom in the choice of a certain number of parameters that can precisely "calibrate" the model. Each symmetry is therefore associated with a set of transformations that frame the "gauge group of the theory". The theory is introduced starting from the Lagrangian formalism developed in the classical mechanism, extending this formalism to classical field theory and finally to quantum field theory.

Lagrangian is defined as the difference between the kinetic energy and the potential energy of the system, as below:

$$\mathcal{L}(q, \dot{q}) = \frac{m}{2}(\dot{q})^2 - V(q) \quad (1.1)$$

and the *action* is defined as  $S = \int dt \mathcal{L}(q, \dot{q})$ .

Using a variational approach it can be shown that for any possible variation of the path of the particle,  $\partial(q)$ , the equation of motion of the system is the one that minimizes the *action*. The results are the so called *Euler-Lagrange* equations:

$$\frac{\mathcal{L}}{\partial q} - \frac{\partial}{\partial t} \frac{\mathcal{L}}{\partial \dot{q}} \quad (1.2)$$

The next step is the extension of the classical mechanics formalism to field theory. One possible way is to generalize the path of a particle which is a function of time  $q(t)$ , into a function of space-time coordinates  $\phi(x)$  which is the vectorial (or tensorial) representation of the field with Lorentz invariance properties of the space-time.

The sub-set of dimension two vectorial representations used in particle physics is called spinors and they are divided into left-handed and right-handed, depending on their chirality:  $\psi_L$  and  $\psi_R$ . The usual representation for Lorentz and parity transformations is the *Dirac* spinor  $\Psi = (\psi_L, \psi_R)$ , which allows to describe properly the dynamics of relativistic particles.

At this point, the Lorentz-invariant Lagrangian is the following:

$$\mathcal{L}_D = \bar{\Psi}(i\gamma^\mu \partial_\mu - m)\Psi \quad (1.3)$$

where  $\gamma$  are an extension of the Pauli matrices into a four dimension space-time and they are called Dirac matrices.

The QFT is also built on the *Noether's* theorem that relates symmetries of the system to conserved observables.

Through this theorem, symmetries become a fundamental building block of the physical theory. A particular set of transformations, called gauge transformations, which by construction leave invariant the Lagrangian of the SM, constitute a building principle of the SM itself.

Let us now consider the global  $U(1)$ <sup>1</sup> transformation of the form:

$$\Psi \rightarrow e^{i\theta}\Psi \quad (1.4)$$

It can be easily demonstrate that  $\mathcal{L}_D$  is invariant under such a transformation and the related conserved observable is the current  $\bar{\Psi}\mu\Psi$ .

However, the Lagrangian is no longer invariant under the transformation:  $\theta \rightarrow \theta(x)$  which means that the gauge invariance is required in each point of the space-time.

The inclusion of an additional field, the photon, which mediates the forces, make the Lagrangian explicitly invariant and it allows to choose a *gauge* of the theory, in fact the action of free electromagnetic field is invariant under  $A_\mu \rightarrow A_\mu - \partial\theta$ , with  $A_\mu$  being the four-vector of the electrostatic and magnetic potential:  $(V, \vec{A})$ .

The above example is useful to understand how the SM is constructed. It is a gauge theory which, analogously to what described in this section, is invariant under:

$$SU(3)_c \otimes SU(2)_L \otimes U(1)_Y \quad (1.5)$$

The  $SU(3)_c$  describes the strong force (see next section) while  $SU(2)_L \otimes U(1)_Y$  term describes the electro-weak sector (see Section 1.1.2). A more detailed discussions follows.

### 1.1.1 Quantum Chromodynamics

The strong interaction between quark and gluons is described by the *Quantum Chromodynamics* (QCD). It is a gauge theory based on non-abelian  $SU(3)_c$ <sup>2</sup> and associated to the three color charges (red, green and blue). A total number of 8 generators  $T^a$  of the group, also called Gell-Mann matrices, represent bosons mediating the force, called *gluons*. They are massless, in contrast with the weak mediators.

The QCD Lagrangian, can be expressed as:

$$\mathcal{L}_{QCD} = \bar{\psi}(i\gamma^\mu D_\mu - m)\psi - \frac{1}{4}G_{\mu\nu}^a G_a^{\mu\nu} \quad (1.6)$$

---

<sup>1</sup> $U(1)$  is the one-dimensional unitary group, i.e. any of its elements can be expressed as a  $1 \times 1$  matrix whose inverse is equal to its transpose conjugate ( $U^{-1} = \bar{U}^*$ ).

<sup>2</sup>S stands for "special", meaning that the group matrices have determinant 1. C stands for "colour", which is the conserved quantity associated with the symmetry

where the index  $a$  represent the 8  $SU(3)_C$  generators,  $\frac{1}{4}G_{\mu\nu}^a G_a^{\mu\nu}$  is the kinetic term of the gluons ( $G^a$  is the gluon field strength tensor) and the covariant derivative  $D_\mu$  is defined as

$$D_\mu = \partial_\mu - ig_s T_a G_\mu^a \quad (1.7)$$

The coupling constant  $\alpha_s$  ( $\frac{g_s^2}{4\pi} \sim 1$ ), is dependent from the transferred momentum  $Q^2$  that correspond to a dependence from the separation between quarks:

$$\alpha_s(Q^2) = \frac{33 - 2n_f}{12\pi} \ln \left( \frac{Q^2}{\Lambda_{QCD}^2} \right) \quad (1.8)$$

where  $n_f$  is the number of quark flavours and  $\Lambda_{QCD}^2$  is the QCD scale parameter, measured to be  $\sim 200$  MeV that sets the scale between different regimes of the theory.

In fact one can discern two cases:

$$\alpha_s(Q^2) \xrightarrow[Q^2 \gg \Lambda_{QCD}^2]{} 0$$

$$\alpha_s(Q^2) \xrightarrow[Q^2 \ll \Lambda_{QCD}^2]{} \infty$$

In the first case, the quark coupling is asymptotically cancelled, in the limit  $Q^2 \rightarrow \infty$ , quarks can be considered as free particles and this phenomena calls *Asymptotic Freedom*. On the contrary, when the separation become relevant, the coupling is so strong to confine quarks in hadronic structures and this different phenomena calls *Confinement*. The only states that occur are completely antisymmetric in the color variables (the color singlets), which is equivalent to saying that the possible compositions of quarks must be "white".

Interaction between particles, that carry charges of color, takes place through the exchange of gluons of the octet, therefore, not only between quarks and gluons but also between gluons and gluons. This is a very important difference between QED (*Quantum Electrodynamics*) and QCD. In QED, in fact, photons have no charge and cannot couple with each other.

### 1.1.2 The electro-weak sector

The first model of the weak interaction was proposed by Fermi in 1933, who proposed an effective field theory at low energies. According to this theory, charged current interactions are approximated by a point-like interaction with a couplig called  $G_F$  [1, 2]. At energies  $\mathcal{O}(100 \text{ GeV})$  the theory breaks and the real propagator of the interaction is the  $W^\pm$  boson.

In 1957, a famous experiment conducted by Wu [3] proved that parity is maximally

violated by the charged weak interaction: it only couples to particles of left-handed chirality (and antiparticles of right-handed chirality). There also exists a neutral weak interaction, which couples both to left-handed and right-handed particles.

This discovery motivated the introduction of the vector-axial (V-A) structure of the Lagrangian of the weak force.

The model of the weak interaction was subsequently promoted to a gauge theory by requiring local invariance under symmetries of the  $SU(2)$  group, and it was associated with a conserved quantity called the *weak isospin*.

Each generation of left-handed fermions forms a doublet satisfying  $I_3 = \pm \frac{1}{2}$ , while right-handed fermions correspond to singlets of null isospin, as follows:

$$\chi_L = \begin{pmatrix} \nu_l \\ l \end{pmatrix}_L \quad l_R \quad (1.9)$$

where  $l = (e, \mu, \tau)$ , and a right-handed neutrino singlet is not introduced since there is still no observation of such a particle. A similar representation is given for quarks where both up ( $u, s, t$ ) and down-types ( $d, c, b$ ) have a right-handed component, singlet under  $SU(2)_L$ .

The transitions between quark doublet members corresponds to  $SU(2)$  raising ( $\tau^+$ ) and lowering ( $\tau^-$ ) operators, giving the charge raising and lowering currents [4]:

$$\begin{aligned} J^+ &\sim g(\bar{u} d_c) = g(\bar{u} \bar{d}_c) \begin{pmatrix} 0 & 1 \\ 0 & 0 \end{pmatrix} \begin{pmatrix} u \\ d_c \end{pmatrix} = g(\bar{q} \tau^+ q) \\ J^- &\sim g(\bar{d}_c u) = g(\bar{u} \bar{d}_c) \begin{pmatrix} 0 & 0 \\ 1 & 0 \end{pmatrix} \begin{pmatrix} u \\ d_c \end{pmatrix} = g(\bar{q} \tau^- q) \end{aligned} \quad (1.10)$$

where overall numerical factors have been omitted, d-quark is 'Cabibbo-rotated' ( $\theta_c \sim 13^\circ$ ) and  $g$  is the dimensionless weak coupling constant and quarks.

If there exist an appropriate symmetry, based on some underlying gauge theory, then a current involving  $\tau_3$  is also expected, since these operators are related via the commutation relation  $[\tau^+, \tau^-, ] = 2\tau_3$ . Hence, with such a gauge theory symmetry, one would expect the existence of a neutral current (identified by the  $Z^0$  boson) of the form :

$$\begin{aligned} J^0 &\sim 2g(\bar{q} \tau_3 q) = g(\bar{u} u - \bar{d}_c d_c) \\ &= g[\bar{u} u - \bar{d}_c d \cos^2 \theta_c - \bar{s}_c s \sin^2 \theta_c - (\bar{d} s + \bar{s} d) \cos \theta_c \sin \theta_c] \end{aligned} \quad (1.11)$$

The terms  $\bar{d}s$  and  $\bar{s}d$  correspond to strangeness-changing neutral currents (SCNC), which are heavily suppressed in nature.

For example, the decay branching ratio  $K^+ \rightarrow \mu^+ \nu_\mu$  is 63.5%, whereas that for  $K_L^0 \rightarrow \mu^+ \mu^-$  is  $\sim 10^{-8}$ .

A mechanism to suppress this unwanted strangeness strangeness-changing neutral currents was suggested in 1970 by Glashow, Iliopoulos and Maiani (GIM) and it will be described in the next section.

### 1.1.2.1 GIM mechanism

Until the beginning of the 1970s, the only three light quarks u, d and s known at this time could explain the observed hadron spectrum and the observed weak decays of pions and kaons were mostly in good agreement with the predictions of the *Cabibbo mechanism*. Glashow, Iliopoulos and Maiani proposed the existence of a second orthogonal doublet, additional to  $(\begin{smallmatrix} u \\ d_c \end{smallmatrix})$ , containing a new quark c (charm) with charge  $\frac{2}{3}$ , as follows [5]:

$$q' = \begin{pmatrix} c \\ s_c \end{pmatrix} = \begin{pmatrix} c \\ -d \sin \theta_c + s \cos \theta_c \end{pmatrix} \quad (1.12)$$

Adding this term gives the total neutral current:

$$\begin{aligned} J^0 &\sim 2g(\bar{q} \tau_3 q + \bar{q}' \tau_3 q') = g(\bar{u}u + \bar{c}c - \bar{d}_c d_c - \bar{s}_c s_c) \\ &= g[\bar{u}u + \bar{c}c - \bar{d}d - \bar{s}s] \end{aligned} \quad (1.13)$$

That is, the unwanted terms cancel, leaving a flavour diagonal result.

The GIM mechanism gives also an estimation of the charmed quark, before the  $J/\Psi$  discovery occurred in 1974.

In the three-quarks picture, and according to the Cabibbo mechanism alone,  $s \rightarrow d$  transitions via *Flavour Changing Neutral Current* FCNC processes would be possible at all orders of the perturbation expansion.

For example, the process  $K_L^0 \rightarrow \mu^+ \mu^-$  FCNC decay could take place, in terms of known quark (u and d-quarks), via the "box-diagram" of Figure 1.1(a).

The calculated rate is larger than what was observed experimentally.

However, including the diagram of Figure 1.1(b), the total amplitude is:

$$\mathcal{M} = \mathcal{M}_{(a)} + \mathcal{M}_{(b)} \sim f(m_u)g^4 \cos \theta_c \sin \theta_c - f(m_c)g^4 \cos \theta_c \sin \theta_c \quad (1.14)$$

Thus, the c-quark induces a cancellation, giving a BR compatible with the experiments, but not a total cancellation because  $m_c \neq m_u$ . Hence, the predictions on the mass of the c-quark that in the end it is  $\sim 3$  GeV. In addition to this major prediction, the GIM mechanism led to the prediction that FCNC processes are forbidden at tree-level Leading Order. The branching ratios of several FCNC decays of the top quark in the SM are given in Table 1.1. The FCNC production is also sensitive to numerous new physics models, as is mentioned in more details in Section 1.3.

The GIM hypothesis represent a generalization of Cabibbo's idea. The introduction of the forth quark (c) restored the symmetry in the (then known) numbers of quark and

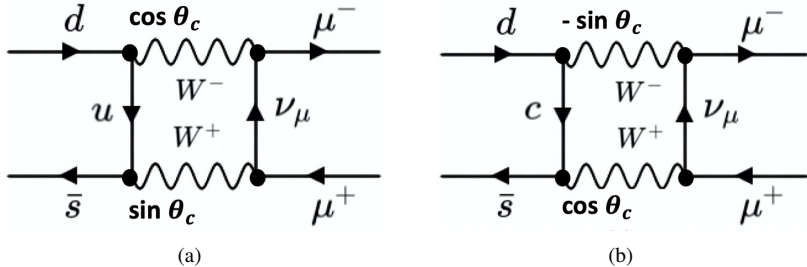


**Figure 1.1** – Feynman diagrams of  $K_L^0 \rightarrow \mu^+ \mu^-$  via (a) u-quark exchange and (b) c-quark exchange

	$t \rightarrow uZ$	$t \rightarrow c\bar{Z}$	$t \rightarrow u\gamma$	$t \rightarrow c\gamma$	$t \rightarrow ug$	$t \rightarrow cg$	$t \rightarrow uH$	$t \rightarrow cH$
BR	$8 \times 10^{-17}$	$1 \times 10^{-14}$	$3.7 \times 10^{-16}$	$4.6 \times 10^{-14}$	$3.7 \times 10^{-14}$	$4.6 \times 10^{-12}$	$2 \times 10^{-17}$	$3 \times 10^{-15}$

**Table 1.1** – Branching ratios for top quark FCNC interactions in the SM [6].

leptons.

These ideas were extended by Kobayashi and Maskawa (1973), who introduced a framework of six quarks and it will be described in the next section.

### 1.1.2.2 CKM matrix

In 1973 Kobayashi and Maskawa extended the Cabibbo's mechanism allowing to describe the transitions within and in-between 3 generations of quarks using the so-called *CKM*  $3 \times 3$  matrix [7, 8], which relates the weak eigenstate of down-type to their mass eigenstate:

$$\begin{pmatrix} d' \\ s' \\ b' \end{pmatrix} = V_{CKM} \begin{pmatrix} d \\ s \\ b \end{pmatrix} = \begin{pmatrix} |V_{ud}| & |V_{us}| & |V_{ub}| \\ |V_{cd}| & |V_{cs}| & |V_{cb}| \\ |V_{td}| & |V_{ts}| & |V_{tb}| \end{pmatrix} \begin{pmatrix} d \\ s \\ b \end{pmatrix} \quad (1.15)$$

By convention, the up-type quarks are taken to be pure states. Therefore, partners of the up-type quarks within the weak isospin doublets are the weak eigenstates  $d'$ ,  $s'$  and  $b'$  which are the pure states.

The CKM matrix is fully defined by 4 independent parameters, which must be determined experimentally. These parameters are: 3 mixing angles and 1 CP-mixing phase, which violates the CP<sup>3</sup> symmetry in the SM [9]. The diagonal elements of the CKM matrix are close to 1, reflecting the fact that transitions are favoured between quarks of the same generation.

The CKM matrix is unitary, i.e. the sum of the transition probabilities for any quark flavour is equal to 1. If this assumption was to be disproved, it could imply the existence

of a fourth quark generation.

## METTERE Electroweak symmetry breaking ???

## 1.2 Top quark physics

The heaviest known elementary particle described by the Standard Model is the top quark.

In 1995, the top quark discovery in FERMILAB [10, 11] was a great success for the SM predictions e.g. the corroboration of existence of a weak isospin partner of the top quark. Due to its large mass, the predicted lifetime  $\tau_t \approx 5 \times 10^{-25}$  s (in agreement with theoretical expectations [12]) entail that it decays before hadronising.

In the next sections, the production mechanism is reported, as well as a dissertation about the decay channels.

### 1.2.1 Production

The top quark can either be produced as pairs, via strong interaction, or as a single top quark via electroweak interaction that does not preserve the flavour.

The main parton sub-processes that lead to top-pair production are the quark-antiquark annihilation ( $q\bar{q} \rightarrow t\bar{t}$ , Figure 1.2(a)) and the gluon-gluon fusion ( $gg \rightarrow t\bar{t}$ , Figures 1.2(b) and 1.2(c)).

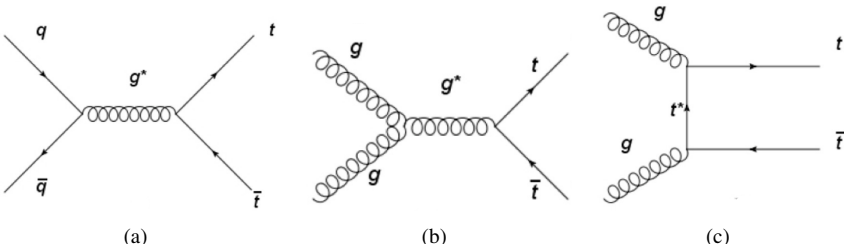


**Figure 1.2 –** Feynman diagrams of  $t\bar{t}$  production via (a) quark-antiquark annihilation ( $q\bar{q} \rightarrow t\bar{t}$ ) and (b,c) gluon-gluon fusion ( $gg \rightarrow t\bar{t}$ )

Since in protons there are not valence antiquarks, the quark-antiquark annihilation is suppressed by the parton distribution functions (PDF) of the antiquark in the proton. Therefore, at LHC the dominant process turns out to be the gluon-gluon fusion, while

<sup>3</sup>Charge transformation followed by a parity transformation.

in a proton-antiproton collider, such as Tevatron, the dominant process is the quark-antiquark annihilation, in fact:

- Tevatron:  $q\bar{q} \rightarrow t\bar{t} \approx 86\%$ ,  $gg \rightarrow t\bar{t} \approx 15\%$
- LHC:  $q\bar{q} \rightarrow t\bar{t} \approx 20\%$ ,  $gg \rightarrow t\bar{t} \approx 80\%$

Top-pairs can be produced also for weak interaction when two quarks exchange  $Z^0$  or a  $\gamma$ ; however the cross-section of these type of processes is negligible when compared to the production cross-section through strong interaction.

Although at LHC the top quarks are mainly produced in the process described above, a not negligible number of tops are produced singly by weak interaction but with a production cross section equal to approximately 1/3 of the top-pair production cross-section, which is, at  $\sqrt{13}$  TeV and taking into account a top quark mass of  $172.5 \text{ GeV}/c^2$ ,  $\sigma_{t\bar{t}} = 831.8^{+19.8+35.1}_{-29.2-35.1} \text{ pb}$  [13].

## 1.2.2 Decay channels

Since the top quark mass is higher than the W boson mass, it decay through weak interaction, mainly in  $t \rightarrow W^+ b$ ; according to SM is 100% of the possible cases.

The other channels ( $t \rightarrow W^+ s$ ,  $t \rightarrow W^+ d$ ) are strongly suppressed by the CKM matrix elements (see Section 1.1.2.2). Exploiting the matrix unitarity and the B meson oscillations it is possible to extract the following BRs[14]:

$$\begin{aligned}\text{BR}(t \rightarrow W^+ b) &\sim 0.998 \\ \text{BR}(t \rightarrow W^+ s) &\sim 1.9 \cdot 10^{-3} \\ \text{BR}(t \rightarrow W^+ d) &\sim 10^{-4}\end{aligned}$$

Therefore, the top decay total width is given by, in good approximation, the decay ( $t \rightarrow W^+ b$ ), thus equals to  $\Gamma_t = 1.44 \text{ GeV}$ . The W boson may decay in only two ways: "leptonically" ( $W \rightarrow l\nu$ ) or "hadronically" ( $W \rightarrow q\bar{q}'$ ). This leads to three different categories of  $t\bar{t}$  decays: dileptonic, semi-leptonic or hadronic. The Figure 1.3 summarise the BRs associated to each channel.

At the hadron colliders, the dominant hadronic mode is the hardest to detect due to the large QCD background.

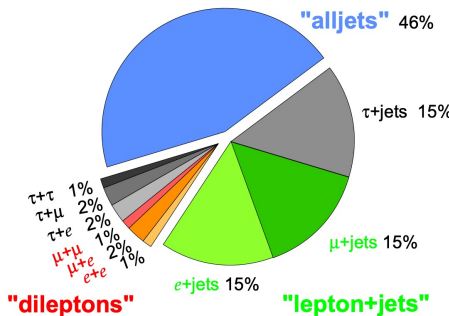


Figure 1.3 – Branching ratios associated to each  $t\bar{t}$  decay channel[15].

## 1.3 Theories for physics beyond the Standard Model

The previous sections describe the core components of what we call *Standard Model* and report few major successes of many. Its predictive power makes this model the most tested in physics and it reaches the culmination of success on 4 July 2012, when the ATLAS and CMS experiments at CERN announced the observation a new particle in the mass region around 125 GeV, the Higgs boson [16].

But in spite of its important achievements, the SM falls short of explaining several important observations that in this section are briefly reported.

SM considers neutrinos as massless particles but this is in contradiction with the results of many experiments, which observed, in several different contexts, the *neutrino oscillations*.

It is a quantum mechanical phenomenon whereby a neutrino created with a specific lepton family number ( $e$ ,  $\mu$ , or  $\tau$ ) can later be measured to have a different lepton family number and this mechanism, implies that the neutrino has a non-zero mass since it arises from mixing between the flavour and mass eigenstates of neutrinos.

SM can not describe *dark matter* and *dark energy*. The first evidence of dark matter came with the observation of the rotational speed of galaxies, which suggests the existence of a huge amount of undetected mass [17].

None of the SM particles could explain this phenomenon and, since a dark matter has never been directly observed implies that it interact only weakly with the ordinary matter and radiation or does not interact at all.

Likewise, dark energy is an unknown form of energy that affects the universe on the largest scales. The first observational evidence for its existence came from supernovae measurements, which showed that the universe does not expand at a constant rate; rather, the expansion of the universe is accelerating.

The data collected by Planck spacecraft, indicate that dark energy contributes 68% of

the total energy in the present-day observable universe. The mass–energy of dark matter and ordinary (baryonic) matter contributes 27% and 5%, respectively, and other components such as neutrinos and photons contribute a very small amount [18].

After the Big Bang one could expect that the universe produced the same amount of particles-antiparticles and that the constant annihilation of pairs would have constituted a universe of radiation. What we observe actually is large cosmological matter (but not antimatter) structures. The mechanism suggested by the SM through the CP-symmetry violation of neutral oscillating hadrons is not sufficient to explain alone this phenomenon.

There are also some other strong indications that the SM could be not yet complete. Indeed, it is based on 19 parameters (excluding neutrino masses) that must be determined experimentally and no known theoretical origin. Moreover, gravity could not be included as a gauge theory because, describing graviton (the associated gauge boson) interactions, the classical theory of Feynman diagrams, and semiclassical corrections with at least two loops lead to *ultraviolet divergences*. These infinite results cannot be removed because quantized general relativity is not perturbatively renormalizable, unlike QED and models such as the Yang–Mills theory. Therefore, when the probability of a particle to emit or absorb gravitons is calculate, the theory loses predictive veracity. Those problems and the complementary approximation framework are grounds to show that a theory more unified than quantized general relativity is required to describe the behavior near the Planck scale.

The problem of *naturalness* is also much debated in literature. The Higgs boson is very sensitive to loop corrections (involving top quark and himself mainly) and if one considers the a theory close to the Planck scale, thus these corrections may explain why the Higgs boson mass is so relatively small compared e.g. with the top quark mass. Another problem is, in fact, the mass scale of fermions that it ranges across many orders of magnitude without any clear explanation.

Many are models of "new physics" that attempt to describe and explain the phenomena mentioned above but so far there is no evidence of new physics Beyond Standard Model (BSM). In the SM, top quark decays almost exclusively into  $bW$  while flavour-changing neutral current (FCNC) decays such as  $t \rightarrow qZ$  are forbidden at tree level. FCNC decays occur at one-loop level (Figure 1.4) but are strongly suppressed by the GIM mechanism (Section 1.1.2.1), with a suppression factor of 14 orders of magnitude relative to the dominant decay mode[19].

However, in the BSM models, the suppression could be relaxed and the loop diagrams mediated by new bosons that could contribute, leading to couplings of many orders of magnitude higher than those expected by the SM.

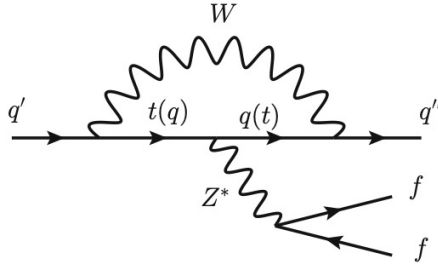


**Figure 1.4** – Sketched Feynman diagram for SM  $q' \rightarrow q'' f \bar{f}$  induced by the  $tqZ$  coupling, where  $q'$  and  $q''$  denote the down-type quarks;  $q = u, c$ , and  $f$  can be any possible fermions. In the Standard Model, FCNC processes are forbidden at tree level but occur at one-loop level (see GIM mechanism in Section 1.1.2.1).

Examples of such extensions are the quark-singlet model (QS)[20], the two-Higgs-doublet model with (FC 2HDM) or without (2HDM) flavour conservation[21], the Minimal Supersymmetric Standard Model (MSSM)[22], the MSSM with R-parity violation (RPV SUSY)[23], models with warped extra dimensions (RS)[24], or extended mirror fermion models (EMF) [25]. Reference [26] gives a comprehensive review of the various extensions of the SM that have been proposed. Table 1.2 provides the maximum values for the branching ratios predicted by these models and compares them to the value predicted by the SM.

In this section we will briefly describe some of these theories interesting for the topics of this thesis.

Model:	SM	QS	2HDM	FC 2HDM	MSSM	RPV SUSY	RS	EMF
$\mathcal{B}(t \rightarrow qZ)$	$10^{-14}$	$10^{-4}$	$10^{-6}$	$10^{-10}$	$10^{-7}$	$10^{-6}$	$10^{-5}$	$10^{-6}$

**Table 1.2** – Maximum allowed FCNC  $t \rightarrow qZ$ , ( $q = u, c$ ) branching ratios predicted by several models[19–26].

### 1.3.1 Quark singlets

The need to suppress the FCNC mechanism lead to two dogmas [27, 28]:

- they are not mediated by  $Z^0$  boson at tree-level
- no FCNC mechanism in the scalar sector at tree-level

It is possible to overcome these dogmas using extensions of the SM, like the Quark Singlets (QS) [29] that introduces a vector-like quark ( $Q = \frac{1}{3}$  or  $Q = \frac{2}{3}$ ), thus a small violation of the  $3 \times 3 V_{CKM}$  unitarity (see Section 1.1.2.2), mediated by  $Z^0$  boson and

natural FCNC suppression at tree-level.

Given  $x_L$  and  $x_R$ ,  $SU(2)_L$  singlets

$$\begin{pmatrix} d' \\ s' \\ b' \\ x' \end{pmatrix} = \begin{pmatrix} |V_{ud}| & |V_{us}| & |V_{ub}| & |V_{ux}| \\ |V_{cd}| & |V_{cs}| & |V_{cb}| & |V_{cx}| \\ |V_{td}| & |V_{ts}| & |V_{tb}| & |V_{tx}| \end{pmatrix} \begin{pmatrix} d \\ s \\ b \\ x \end{pmatrix} \quad (1.16)$$

The non orthogonality of the columns leads to terms of the type:

$$J_\mu = \frac{g}{\cos\theta_W} Z_{bd} \bar{b}_L \gamma_\mu d_L Z^\mu \quad (1.17)$$

where

$$Z_{bd} = V_{ud} V_{ub}^* + V_{cd} V_{cb}^* + V_{td} V_{tb}^* \quad (1.18)$$

and  $Z_{bd}$  is suppressed by  $\frac{m_q}{m_x}$ .

In this way is possible to have deviations from  $3 \times 3$  unitarity.

The PMNS matrix in the leptonic sector, in the context of see-saw mechanism is not  $3 \times 3$  unitarity [30].

Vector-like quarks provide the simplest model with spontaneous *CP violation* and a framework to have a common origin of all CP violation because it is a potential solution of the *strong CP problem* without involving other particles, e.g. axions.

### 1.3.2 Two Higgs Doublet Model

The LHC discovery of a Standard-Model-like Higgs  $H(125)$  particle in 2012[16] could be a portal to an extended Higgs sector predicted by several models, one of this is the Two-Higgs-Doublet Model (2HDM) [31]. The most natural extension of the Standard Model scalar sector is the addition of an extra  $SU(2)_L$  doublet.

The 2HDM is an *Effective Field Theory* (EFT<sup>4</sup>) consisting of two complex Higgs doublets, which provide masses to both the up-type and the down-type fermions:

$$\Phi_1 = \begin{pmatrix} \phi_1^+ \\ \phi_1^0 \end{pmatrix} \quad \Phi_2 = \begin{pmatrix} \phi_2^+ \\ \phi_2^0 \end{pmatrix} \quad (1.19)$$

with the minimum of the potential corresponding to

$$\Phi_{1,0} = \frac{1}{\sqrt{2}} \begin{pmatrix} 0 \\ \nu_1 \end{pmatrix} \quad \Phi_{2,0} = \frac{1}{\sqrt{2}} \begin{pmatrix} 0 \\ \nu_2 \end{pmatrix}. \quad (1.20)$$

---

<sup>4</sup>An EFT corresponds to a low-energy approximation to a more fundamental underlying theory, characterized by an energy scale  $\Lambda$  (e.g. the mass of new particles)

After the electroweak symmetry breaking (EWSB), there are five physical scalar fields, consisting of neutral bosons  $h, H, A$  of which the first two bosons are CP-even, opposed to the  $A$ -boson which is CP-odd and of two charged Higgs states  $H^\pm$ .

The model is parametrised by the five Higgs masses ( $m_H, m_h, m_{H^\pm}, m_A$ ), the ratio of the vacuum expectation values of the two Higgs doublets  $\tan \beta = \nu_2/\nu_1$  and the mixing angle  $\alpha$  between the CP-even Higgs states.

There exist four types of 2HDM which simultaneously forbid the presence of FCNC and preserve CP symmetry:

- in Type I all fermions couple to the second doublet  $\Phi_2$ . It follows that BR are independent of  $\tan \beta$ ;
- in Type II or MSSM-like scenario, lepton and down-type quarks couple to the first doublet  $\Phi_1$ , whilst up-type quarks couple to  $\Phi_2$ ;
- in Type III or lepton specific scenario, quarks couple to  $\Phi_2$  while leptons couple to the other doublet;
- in Type IV or flipped model, the coupling of the leptons is reversed with respect to the Type-II model.

### 1.3.3 Minimal Supersymmetric Standard Model

The FCNC processes have also been studied with the *Minimal Supersymmetric Standard Model* (MSSM), where loop corrections of the supersymmetric QCD with gluinos and scalar quarks, as shown in Figure 1.5. In supersymmetric QCD it was shown that there occur flavour-changing strong interactions between the gluino, the left-handed quarks, and their supersymmetric scalar partners, whereas the couplings of the gluino to the right-handed quarks and their partners remains flavour diagonal. To calculate the one-loop diagrams shown in Figure 1.5 we need the couplings of the gluon to the gluinos, of the scalar partners of the left-handed quarks to the gluon, photon, and Z boson, and of the gluino to the left-handed quark and its scalar partner.

After the introduction of non-trivial squark mixing, is possible to calculate the coupling that leads to flavour changing in which appears  $K_{ij}$ , the supersymmetric version of  $V_{CKM}$ :

$$\begin{pmatrix} 1 & \epsilon & \epsilon^2 \\ -\epsilon & 1 & \epsilon \\ -\epsilon^2 & -\epsilon & 1 \end{pmatrix} \quad (1.21)$$

It is possible to demonstrate that all divergent terms cancel exactly, without the GIM mechanism.

Finally, we define  $\mathcal{B}(t \rightarrow cZ) = \frac{\Gamma_S(t \rightarrow cZ)}{\Gamma_W(t \rightarrow bW)}$ , where:

$$\Gamma_W(t \rightarrow bW) = \frac{\alpha}{16 \sin \Theta_W} m_{top} \left(1 - \frac{m_W^2}{m_{top}^2}\right)^2 \left(2 + \frac{m_{top}^2}{m_W^2}\right) \quad (1.22)$$

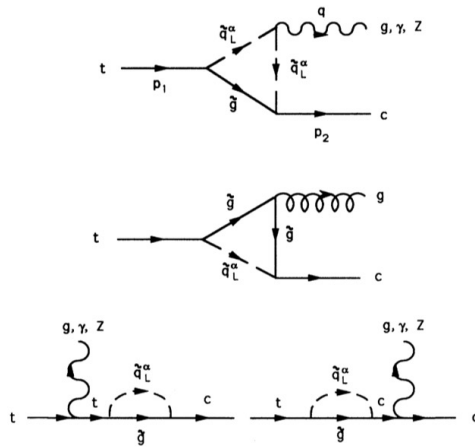


**Figure 1.5** – The diagrams with scalar quarks and gluinos within the loop, which contribute to the top quark decay into a charm quark and a Z boson, photon, or gluon[32].

Using the following values for the parameters  $m_{top} = 174 \text{ GeV}$ ,  $\alpha_s = 1.4675 / \ln \left( \frac{m_{top}^2}{\Lambda_{QCD}^2} \right)$  with  $\Lambda_{QCD} = 0.18 \text{ GeV}$ , is possible to see the branching ratio  $\mathcal{B}(t \rightarrow cZ)$  as a function of the scalar mass  $m_S$  for a gluino mass of 100 GeV (Figure 1.6).

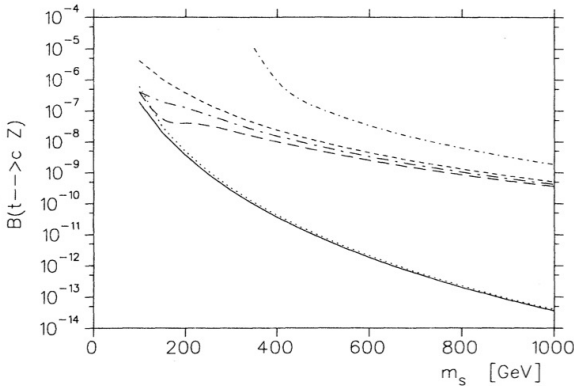


**Figure 1.6** – The branching ratio  $\mathcal{B}(t \rightarrow cZ)$  as a function of the scalar mass  $m_S$ . The gluino mass was taken to be 100 GeV. The solid line is the unphysical case with no squark mixing, the dotted lines are different scenarios of squark mixing[32].

We see that without mixing,  $\mathcal{B}(t \rightarrow cZ)$  decreases rapidly with increasing scalar mass. The mixing has a drastic effect. It enhances the branching ratio by up to 5 orders of magnitude for large  $m_S$ .

# CHAPTER 2

---

## The LHC accelerator and the ATLAS experiment

---



**Figure 2.1** – The LHC ring, aerial view.

This chapter main focus is the experimental setup, thus the ATLAS detector, one of the four large experiments at CERN (*Conseil Européen pour la Recherche Nucléaire*) and shown in Figure 2.1.

Established in 1954, CERN is the largest particle physics laboratory in the world and the organization is based in a north-west suburb of Geneva on the Franco-Swiss border. The analysis presented in this thesis is based on the data collected in the 2015, 2016, 2017 and 2018. Since December 2018, LHC has been shut-down (LS2, 2019-2020) to undergo a major upgrade (Phase I Upgrade) which may enable to collect up to  $300 \text{ fb}^{-1}$  at a c.o.m. energy of 14 TeV until 2023. After that, a second major upgrade (Phase II Upgrade) is planned to the LHC (LS3, 2014-2025) which will increase the interaction rate by a factor of 10; this upgrade will lead LHC to High-Luminosity LHC (HL-LHC).

## 2.1 The LHC accelerator

Located at CERN, the Large Hadron Collider (LHC) [33]. is the world's highest energy particle accelerator. LHC is a circular hadron accelerator, positioned at a depth of about 100 m in the tunnel built for the LEP accelerator, at CERN in Geneva. It is 26.6 km long and currently operates by making proton beams collide at an energy  $\sqrt{s} = 13$  TeV.

CERN's choice to replace the LEP leptonic collider with an hadronic one, such as LHC, has brought two fundamental advantages: the first is that for the same infrastructural size it is possible to reach a higher energy in the center of mass, since the energy lost by radiation of synchrotron from a particle in circular motion is  $\frac{dE}{dt} \propto \frac{E^4}{m^4 R}$ , where  $R$  is the bending radius and  $m$  is the mass of the accelerated particle travelling at an energy  $E$ . The second advantage is that the composite structure of the protons allows access to a wider energy spectrum that can be explored simultaneously without having to change the beam parameters. On the other hand, the number of events considered as a background also increases. In addition to proton-proton (p-p) collisions, at LHC collisions between heavy lead ions (Pb-Pb) also occur .

Before reaching the highest possible energy at the LHC, the protons undergo subsequent acceleration steps. The overall accelerator complex is shown in Figure 2.2.

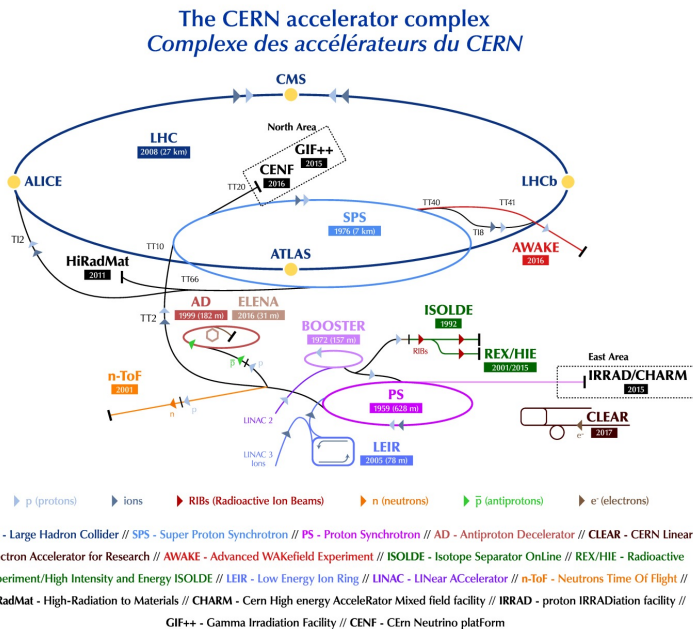


**Figure 2.2 –** The overall CERN accelerator complex [34].

The first step is the proton production from hydrogen gas and they are accelerated up to 50 MeV at the LINear ACcelerator 2 (LINAC 2). These protons are then injected into the Proton Synchrotron Booster (PSB) where their energy reach 1.8 GeV. The acceleration chain continues into the Proton Synchrotron (PS) which pushes the beam to 25 GeV. After that, the beam is injected into the Super Proton Synchrotron (SPS) where the protons are accelerated up to 450 GeV. Finally, the bunches of protons are injected in the LHC. A typical bunch train corresponds to 2808 bunches for each beam with 25 ns separation and bunch contains about  $10^{11}$  protons) colliding at a rate up to 40 MHz. The LHC is designed to accelerate each beam at an energy of 7 TeV thanks to a complex system of dipole and higher order magnets but the LHC performance has not always been those observed to the present day.

The first protons beams circulated in the LHC for the first time in September 10<sup>th</sup> of 2008. From 2010 to 2012, the protons beams had an energy of 3.5 TeV. From 2012 to 2013, the energy reached was 4 TeV per beam. The first shutdown ended when the LHC started to accelerate beams up to an energy of 6.5 TeV in April 5<sup>th</sup> of 2015.

Since protons are charged particles, a strong magnetic field, produced by 1232 superconducting electromagnets, curve the beams around the circular accelerator. To maintain the superconductivity properties, these magnets requires a temperature of 1.9 K ( $\approx 271.3$  °C). This temperature allows this dipole magnets to generate a magnetic field of 8 T. Besides this magnets, a total of 392 quadrupole magnets maintain the beams focused and 16 radiofrequency cavities accelerate particles and keep them in controlled bunches with an constant energy. Four main interaction points are used as collisions points corresponding to the location of the four detectors: ALICE, ATLAS, CMS and LHCb.

The beam in the LHC is not continuous but rather divided in a collection of protons (bunches) colliding at a rate up to 40 MHz. The LHC beam at full intensity nominally consists of 2808 bunches and each bunch contains  $\approx 1.15 \times 10^{11}$  protons, spaced by 25 ns.

The number of multiple interactions per bunch crossing is called *pile-up* and it is denoted by  $\mu$ . Actually there are two different sources of pile-up:

- in-time pile-up occurs when multiple collisions take place in a single bunch crossing
- out-of-time pile-up is due to finite read-out time resolution of the detectors, often larger than 25 ns. In this case, the residual energy from a previous bunch crossing could potentially be associated to the following bunch crossing.

The distribution of  $\langle \mu \rangle$  is shown in Figure 2.3, for the different data-taking periods. The average pile-up for 2015-2018 is  $\langle \mu \rangle = 33.7$ .

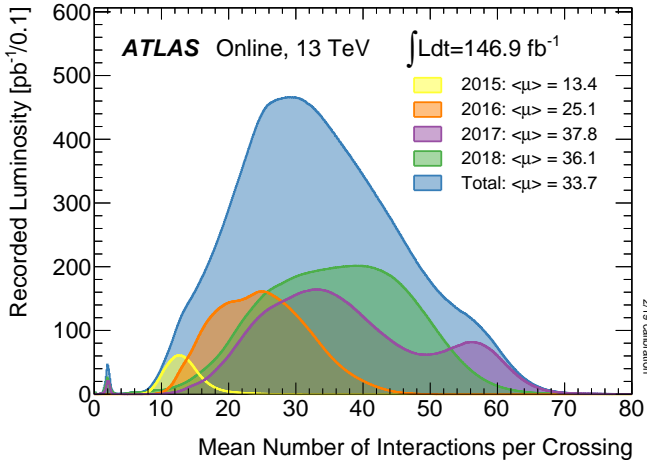


**Figure 2.3** – Luminosity-weighted distribution of the mean number of interactions per crossing for the 2015-2018 pp collision data at  $\sqrt{13}$ . All data recorded by ATLAS during stable beams is shown, and the integrated luminosity and the mean  $\mu$  value are given in the figure [35].

The event rate of a given process with cross section  $\sigma$  is given by  $\frac{dN}{dt} = \mathcal{L}\sigma$ , where  $\mathcal{L}$  is a characteristic of the accelerator, known as *instantaneous luminosity* and is given by:

$$\mathcal{L} = \frac{N_b^2 k_b f \gamma}{4\pi \sigma_x \sigma_y} F \quad (2.1)$$

where  $N_b^2$  is the number of particles per bunch,  $k_b$  is the number of bunches,  $\gamma$  represents the relativistic gamma factor,  $f$  is the revolution frequency of the accelerator,  $\sigma_x$  and  $\sigma_y$  are the horizontal and vertical beam size,  $F$  is a geometrical correction factor from the crossing-angle of the two beams at the interaction point (IP).

Given a period of time  $T$ , one can define the *integrated luminosity* as  $L = \int_0^T dt \mathcal{L}$  which is typically expressed in  $\text{fb}^{-1}$  (1 b =  $10^{-28} \text{m}^{-2}$ ).

Figure 2.4 shows the total integrated luminosity over the full LHC data taking period at  $\sqrt{13}$  TeV and Table 2.1 summarise the main design parameters of LHC.

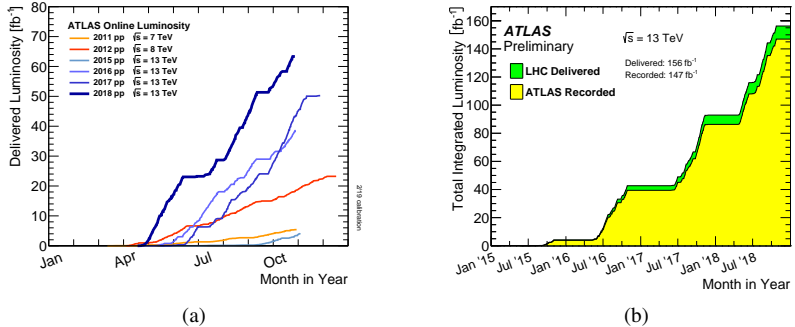


**Figure 2.4** – Cumulative luminosity versus (a) day delivered to ATLAS during stable beams; (b) time delivered to ATLAS (green) and recorded by ATLAS (yellow) during stable beams for pp collisions at  $\sqrt{13}$  [35].

Parameter	2015	2016	2017	2018
Bunch intensity [ $\times 10^{11}$ p]	1.2	1.1	1.25	1.15
Number of bunches	2200	2200	1900	2500
Emittance [ $\mu\text{m}$ ]	3.5	2.5	2.0	2.2
Crossing angle [ $\mu\text{rad}$ ]	290	280	300	300
Peak luminosity [ $10^{34}\text{cm}^2\text{s}^{-1}$ ]	0.5	1.5	1.5	2.0

**Table 2.1** – Main beam parameters of proton-proton collisions of LHC in Run2.

## 2.2 The ATLAS detector

ATLAS (A Toroidal LHC ApparatuS) [36] is a multi-purpose apparatus whose primary goal is to identify and measure the properties of particles produced in p-p collision. The overall ATLAS detector layout is shown in Figure 2.5.

The ATLAS detector consist of a concentric cylinder shape ( $4\pi$  coverage), therefore nominally forward-backward symmetric with respect to the interaction point (IP) where the proton beams collide in it. It can be divided into five main parts:

- Magnet System (section 2.2.1);
- The Inner Detector (section 2.2.2);
- The Calorimetric System (section 2.2.3);
- Muon Spectrometer (section 2.2.4).
- Trigger and data acquisition System (section 2.2.5).

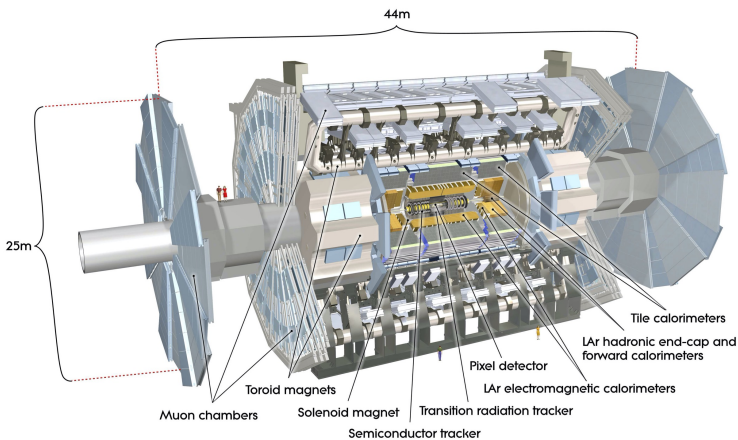


**Figure 2.5 – Cut-away view of the ATLAS detector.** The dimensions of the detector are 25 m in height and 44 m in length. The overall weight of the detector is approximately 7000 tonnes [36].

## Coordinate system

The ATLAS coordinate system is a right-handed Cartesian coordinate system with the origin defined at the IP, in the center of the detector.

The  $z$ -axis corresponds to the beam pipe while the  $x$  and  $y$  directions define the transverse plane.

A cylindrical coordinate system is often used due to the geometry of the detector, where  $\phi$  is the azimuthal angle and  $\theta$  is the polar angle.  $\phi$  is orthogonal to the beam direction, therefore it is invariant under a Lorentz boost( $z$ -axis), while  $\theta$  is not an invariant, so the *pseudorapidity* is defined as:

$$\eta = -\ln \left( \tan \left( \frac{\theta}{2} \right) \right) \quad (2.2)$$

Pseudorapidity is an approximation of the *rapidity*<sup>1</sup> for relativist particles ( $m \ll p$ ). The distance between two objects is indicated using  $\Delta R$ , defined as:

$$\Delta R = \sqrt{\Delta\eta^2 + \Delta\phi^2} \quad (2.3)$$

The transverse momentum is the projection of the momentum orthogonal to the beam direction is defined as:

$$p_T = \sqrt{p_x^2 + p_y^2} \quad (2.4)$$

<sup>1</sup>Rapidity is defined as  $y = \frac{1}{2} \ln \frac{E+p_z}{E-p_z}$

## 2.2.1 Magnet system

The magnet configuration comprises a thin superconducting solenoid surrounding the inner-detector cavity, and three large superconducting toroids (one barrel and two end-caps) arranged with an eight-fold azimuthal symmetry around the calorimeters. This fundamental choice has driven the design of the rest of the detector.

The inner detector is immersed in a 2 T solenoidal field provided by the central solenoid with inner radius of 1.23 m and a total length of 5.8 m.

It is designed to minimize the amount of material in front of the calorimeter to have a small impact on the energy measurement. This is achieved by hosting the solenoid and the cryostat in the same vacuum vessel of the electromagnetic calorimeter.

The overall dimensions of the magnet system is 26 m long and 20 m diameter and provide and average magnetic field intensity of 0.5 T in the barrel and 1 T in the end-caps regions [37].

## 2.2.2 The inner Detector

The Inner Detector (ID) [36] is the detector system closest to the beam.

It is composed of three detectors: the semiconductor pixel detector (PIXEL), the microstrip detector SCT (Semi-Conductor Tracker), and the most external, the transition radiation detector TRT (Transition Radiation Tracker).

Its overall layout is depicted in Figure 2.6.

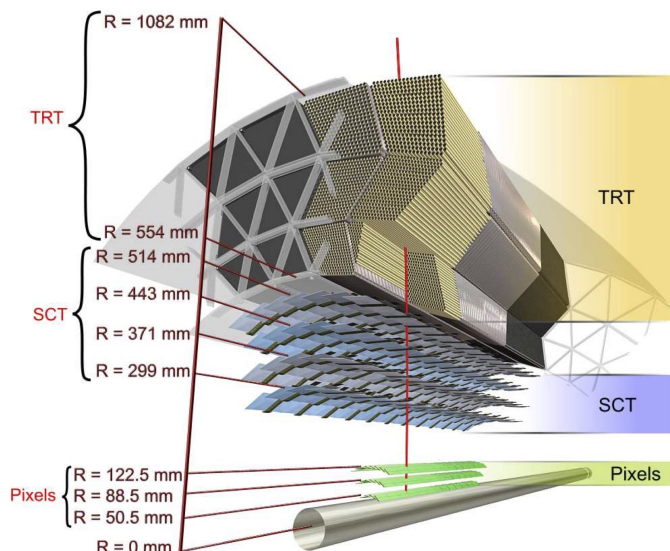


**Figure 2.6 – Schematic view of the barrel of the ATLAS inner tracking system [36].**

The ID is contained in a cylinder 7 m long and 1.15 m in radius, placed in a 2 T solenoid magnetic field and it is designed to trace charged particles with a minimum moment of 0.1 GeV/c to allow the measurement of the moment through the curvature radius and the reconstruction of the main interaction and decay vertices (both primary and secondary). The innermost part of the ID, which has a radius of about 15 cm, consists of silicon pixels to maximize the precision in the reconstruction of the tracks and the resistance to radiation. The pixel detector records on average three points for each track, which allows a reconstruction of the secondary decay vertices. This detector has a total of approximately 80 million sensitive elements.

The intermediate part, which covers a radius ranging from 30 to 60 cm, uses a microstrip detector (Semi-Conductor Tracker), to provide good spatial resolution. The detection technique of the SCT relies on the same principle as for the pixel detector, however long strips are used compared to the rectangular pixels due to the smaller particle density in the outer layers. It is built around the Pixel detector and is designed to provide eight precision measurements per track, contributing to the measurements of momentum, impact parameter and vertex position. The total number of sensitive items is around 6 million.

The outermost layer ranges from 60 to 95 cm in radius; it is a gas detector (Transition Radiation Tracker) consisting of a set of small diameter tubes, containing Xe (70%), CO<sub>2</sub> (27%), O<sub>2</sub> (3%); it provides a good resolution of the curvature of the track and contributes strongly to its reconstruction.

The tracker contributes to the identification of the electrons, being sensitive to the emission of transition radiation that the particles emit when passing between different materials.

### 2.2.3 The Calorimetric System

Calorimeters must provide good containment for electromagnetic and hadronic showers, they must limit punch-through into the muon system, and finally they must detect the particles that do not lose energy by ionization and are therefore not seen by the internal detector.

It is important that calorimeters cover most possible portion of solid angle; in fact, if a particle pass through a region without instrumentation, it is not detected and its energy contributes to the *Missing Transverse Energy* (MET), the precision of which is essential for identifying and studying weakly interacting particles such as neutrinos and possibly, new BSM particles.

In ATLAS there are two calorimeters: the Electromagnetic Calorimeter (ECAL) and the Hadron Calorimeter (HCAL), as depicted in Figure 2.7 and they cover the range  $|\eta| < 4.9$ .

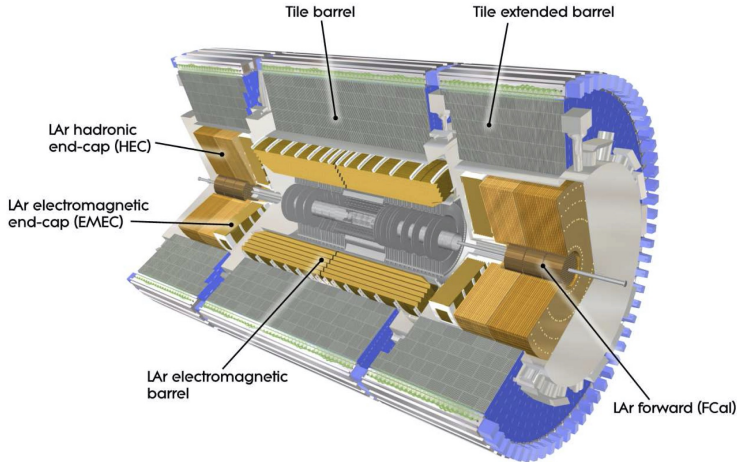


**Figure 2.7** – Cut-away view of the ATLAS calorimeter system [36].

The ECAL is divided into a barrel part ( $|\eta| < 1.475$ ) and two end-cap components ( $1.375 < |\eta| < 3.2$ ), each housed in their own cryostat.

It is a lead-LAr detector with accordion-shaped kapton electrodes and lead absorber plates over its full coverage. The accordion geometry provides complete  $\phi$  symmetry without azimuthal cracks. The lead thickness in the absorber plates has been optimised as a function of  $\eta$  in terms of ECAL performance in energy resolution.

A schematic representation of the ECAL in the barrel and its main construction parameters are shown in Figure 2.8.

The outer calorimeter is the HCAL, which is divided in Tile Calorimeter (TileCal), the Hadronic End-cap Calorimeter (HEC) and the Forward Calorimeter (FCal).

LAr technology is also used for the hadronic calorimeters, matching the outer  $|\eta|$  limits of end-cap electromagnetic calorimeters. The tile calorimeter barrel covers the region  $|\eta| < 1.0$ , and its two extended barrels the range  $0.8 < |\eta| < 1.7$  and it is a sampling calorimeter using steel as the absorber and scintillating tiles as the active material.

The HEC consists of two independent wheels per end-cap, located directly behind the end-cap electromagnetic calorimeter and the technology is similar to that of the electromagnetic one in the end-cap region, the active medium is LAr, but the absorption medium is made of copper rather than lead. The FCal ( $3.1 < |\eta| < 4.9$ ) is integrated into the end-cap cryostats, as this provides clear benefits in terms of uniformity of the calorimetric coverage as well as reduced radiation background levels in the muon spectrometer. The FCal consists of three modules in each end-cap: the first, made of copper, is optimised for electromagnetic measurements, while the other two, made of tungsten, measure predominantly the energy of hadronic interactions.

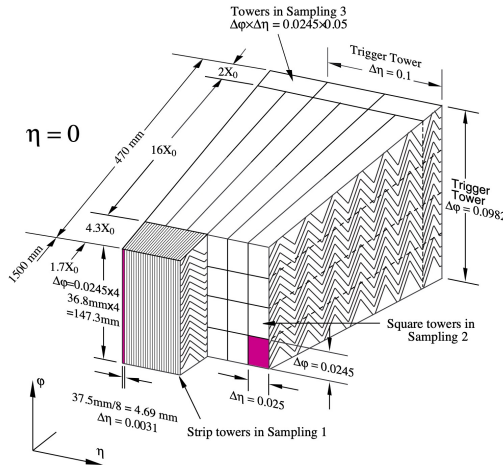


**Figure 2.8 – Sketch of the accordion structure of the ECAL [38].**

An important quantity to mention is the energy resolution which is parameterized as:

$$\frac{\sigma_E}{E} = \frac{S}{\sqrt{E}} \oplus \frac{N}{E} \oplus C \quad (2.5)$$

The first term represent the stochastic contribution related to the shower evolution, the second term is related to the read-out electronics and the effect of the pile-up. The last term is a constant, due to systematic effects (e.g. mis-calibrations, dead detector material). The dominant source of uncertainty is linked, at low energy, with the high pile-up whereas, at high energy, C becomes the leading uncertainty.

## 2.2.4 Muon spectrometer

The calorimeter is surrounded by the Muon Spectrometer (MS) depicted in Figure 2.9, which is placed at the outermost part of the ATLAS detector.

The outer layers are reached by a few types of particles, mainly muons and neutrinos. Those muons ionise with the materials passed through since they are charged particles but the energy, that muons lose by the electromagnetic interaction with other nuclei, is not such as to brake them until absorption. However the MS identify them and measure their momentum.

A series of magnets arranged externally to the calorimeter creates a toroidal-shaped magnetic field that modify the charged particles direction allowing the measurement of the momentum. For muons with  $p_T > 30$  GeV the measurement is much more precise than the measurement obtained by the internal detector. For lower  $p_T$ , on the other hand, the measurement is less accurate, due to the energy loss in the previous layers of

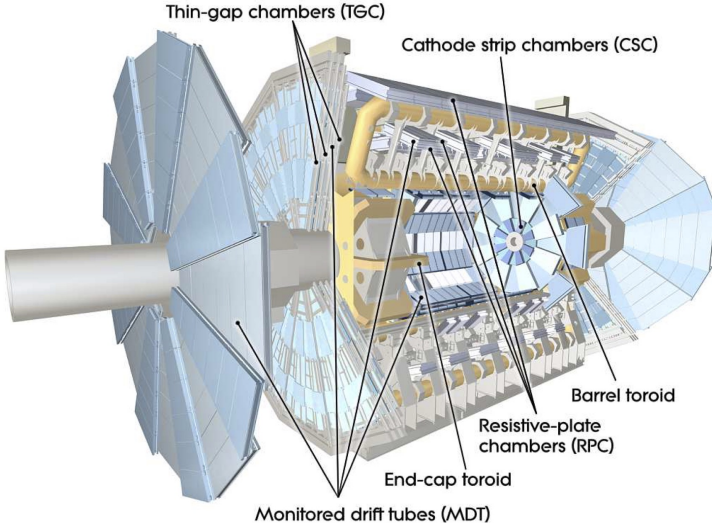


**Figure 2.9** – Cut-away view of the ATLAS muon system [36].

the detector and taken in to account to handle *soft muons*, presented in Chapter 4. For both the central part and the end-caps, there are two types of detectors:

- a trigger system based on cameras with fast response, such as the *Resistive Plate Chamber* (RPC) and the *Thin Gap Chamber* (TGC),
- precision tracking chambers, such as the *Monitored Drift Tube* (MDT) and the *Cathode Strip Chamber* (CGS).

In the central region ( $|\eta| < 1.05$ ), the RPCs consist of two parallel planes filled with a mixture of gas that ionises when a muon passes. The HV applied between the plates allows the development of avalanches, along the ionization track towards the anode, which constitutes a signal.

In the end-cap ( $1.05 < |\eta| < 2.4$ ), TGCs are used to complement the RPCs in the triggering system for their good time resolution and rate capability.

The TGC is a multi-wire proportional chamber operated in a highly quenching gas mixture. Both TGCs and RPCs can achieve a read-out time  $< 25$  ns [39].

MDTs are used for muons with  $|\eta| < 2$  and they are a series of aluminium tubes, filled with a gas mixture of Argon and CO<sub>2</sub>. A central wire serving as anode allows to collect the ions that are formed following the passage of the muon into the gas.

CSCs cover the area where  $2 < |\eta| < 2.7$  and are radially oriented proportional multi-wire chambers, i.e. metal chambers containing a system of parallel and perpendicular anodic wires with strips of opposite polarity.

One important point to stress is that this detector measures the characteristics of any charged particle that passes through it and not just muons. For this reason it is possible that other particles that are not muons, such as pions that manage to overcome the calorimeter and detected as muons.

An estimation of fake soft muons rate is discussed in the Section ?? . What is presented in this paragraph about the MS is a general overview but much more will be presented in Chapter ,going deeper on its functioning and its upgrade for HL-LHC.

## 2.2.5 ATLAS trigger and data acquisition

Once fully operational, with the high frequency of collisions typical at LHC, an impressive amount of data is produced (40 MHz of p-p bunch collision frequency), which would be impossible to manage without the application of filters. However, the *Trigger and Data Acquisition system* (TDAQ) is able to recognize the interesting events for the study of ATLAS physics.

In Run2 the trigger system consists of two levels of event selection: the *Level-1 trigger* (L1), an hardware trigger that reduces the rate to 100 kHz and a *High-Level Trigger* (HLT), a software trigger, further reducing event rate to 1 kHz.

The Level-1 trigger is composed by three subsystem: the first is the L1 calorimeter trigger (L1Calo), which uses calorimeter information; the second is the L1 muon trigger (L1Muon), which primarily uses TGC and RPC information to make fast decisions on muon items; the third is the L1 topological trigger (L1Topo) that combines information from L1Calo and L1Muon and the Central Trigger Processor (CTP) makes the final decision.

At this point, L1 identifies the *Region of Interest* (RoI) with an event rate reduced below 100 kHz. The RoI are then used by the HLT, which has access to the information of all the sub-detectors, targeting the average rate at 1 kHz.

Finally, the events are assembled into an event record passing to the offline storage facilities for a complete off-line reconstruction [40].

# CHAPTER 3

## The Trigger system upgrade for High-Luminosity LHC

Since the beginning, the LHC accelerator has faced operating periods and dedicated shut-downs to upgrade the accelerator machine and the detectors. In Figure 3.1 a summary of the LHC timeline for operation and upgrade is shown.

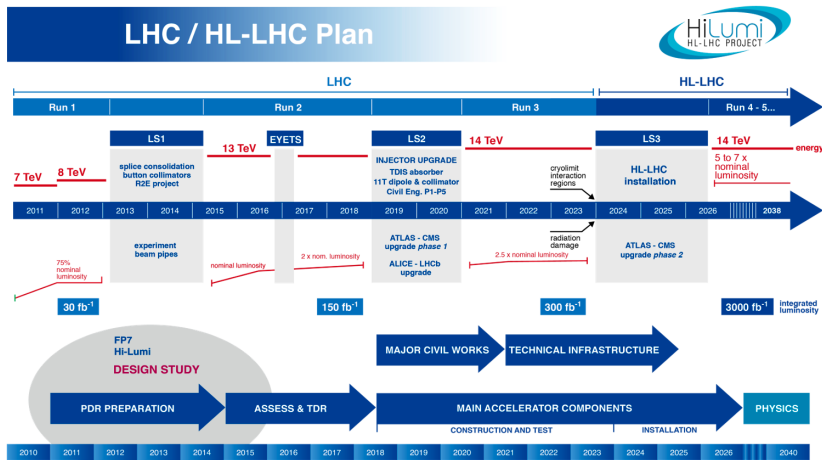


**Figure 3.1 – Summary of the LHC timeline for operation and upgrade [41].**

At the end of 2018, the LHC was shut-down and for two years it will be upgraded to

reach the center-of-mass energy to its design value of 14 TeV and collect  $300 \text{ fb}^{-1}$  of data, almost double of the current available statistics of Run2.

After 4 years of duty cycle, the High-Luminosity period of LHC (HL-LHC) will start and aims to bring the integrated luminosity to  $3000 \text{ fb}^{-1}$ , unlocking several studies, mostly related with rare phenomena, which are impossible to perform with the current statistics.

The main focus of this chapter is the trigger system upgrade for HL-LHC and several studies will be presented.

### 3.1 ATLAS Barrel Muon Trigger

The muon detector chambers are arranged such that particles from the interaction point traverse three stations of chambers.

The system is subdivided azimuthally into 16 sectors numbered from 1 to 16. The sector number increases in the direction of increasing  $\phi$  with the number 1 corresponding to coordinate  $\phi = 0$ . The odd sector (called “large sectors”) are located between barrel coils, instead, the even sectors (called “small sectors”) are covered by the coils.

The muon spectrometer consists of three large air-core superconducting toroidal magnets (two end-caps and one barrel) providing a field of approximately 0.5 T.

In the barrel, the chambers are arranged in three concentric cylinders around the beam axis called BI (Barrel Inner), BM (Barrel Middle), and BO (Barrel Outer).

RPC planes are installed in the Middle and Outer stations of the Muon Spectrometer always mechanically associated with MDT precision chambers (except for some “special” chambers).

Two RPC planes are integrated with MDT in the Middle stations and one RPC plane only in the Outer stations.

Schematic drawings of the present ATLAS MS [42], are shown in Figures 3.2 and 3.3. The MS detector and electronics components have been designed for 10 years of operation at a luminosity of  $1 \times 10^{34} \text{ cm}^{-2} \text{ s}^{-1}$ , corresponding to an integrated luminosity of  $1000 \text{ fb}^{-1}$ . Conservative safety factors for radiation tolerance and rate capability were taken into account in the original designs, and components have been tested up to and above levels corresponding to the expected doses and rates predicted by simulations multiplied by the safety factors. After the start of LHC operation, detector hit rates and radiation doses could be measured directly, and the previous simulations have been found to agree with the measurements to within a maximum deviation of about 50%.

Based on this observation, the original safety factors were reduced [10], and as a consequence the original irradiation and high-rate tests have qualified the detectors for longer running and higher rates than originally anticipated.

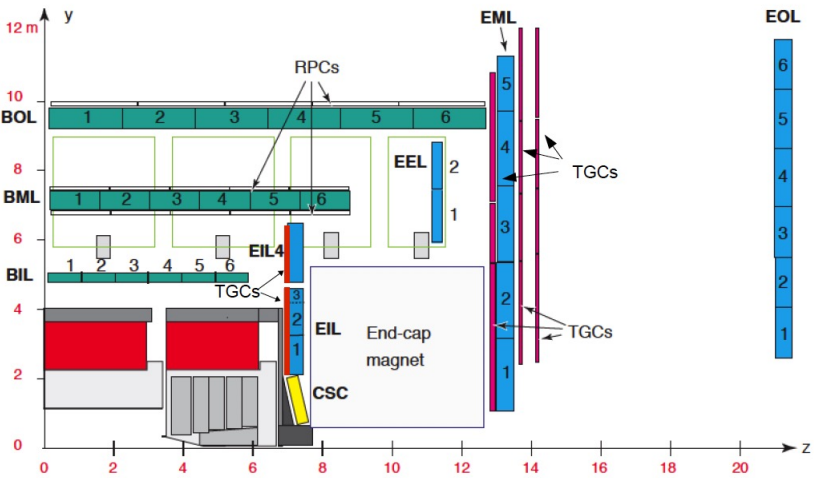
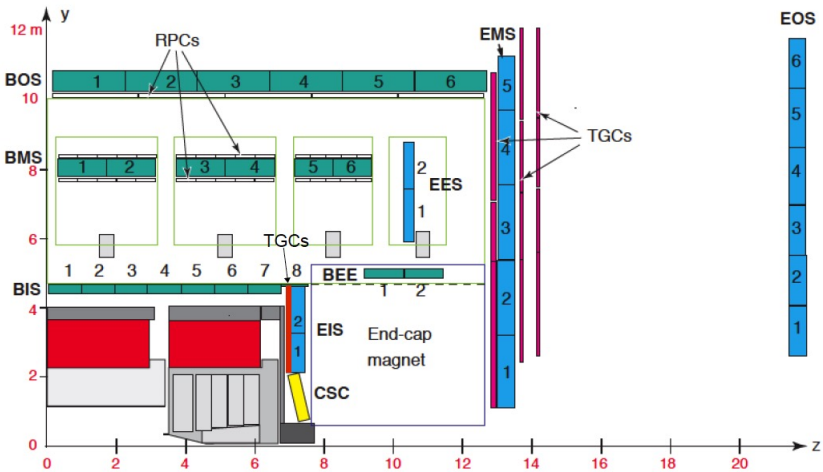


**Figure 3.2 –** Two R-Z views of the present (Run 1/2) ATLAS muon spectrometer layout. Top: One of the azimuthal sectors that contain the barrel toroid coils (small sector). Bottom: One of the sectors in-between the barrel toroid coils (large sector) [42].

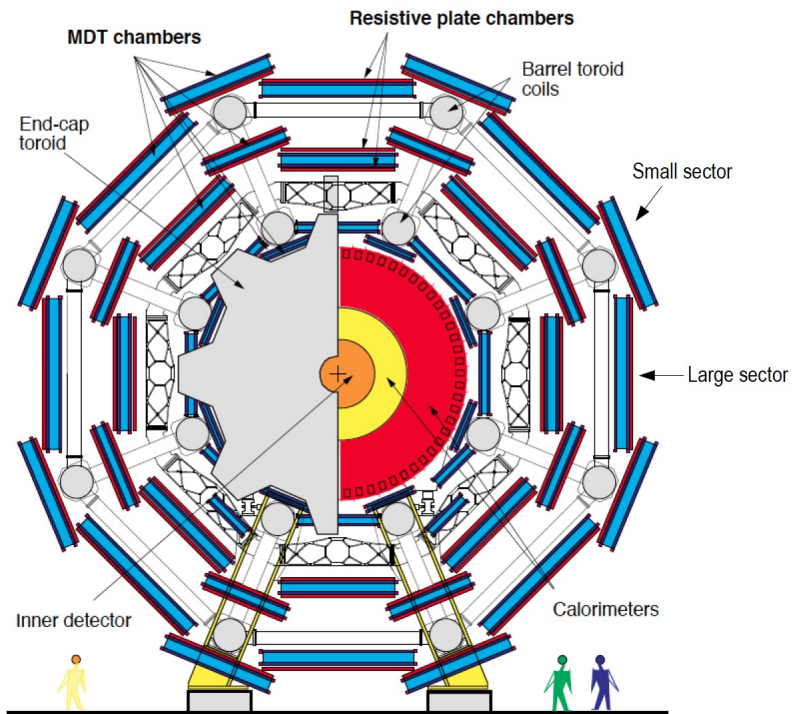


**Figure 3.3 –** View of the present (Run 1/2) ATLAS muon spectrometer barrel layout in the plane transverse to the beam axis (X-Y plane) [42].

## 3.2 BI upgrade for Phase II

In the Phase-I upgrade, foreseen for LS2, the Small Wheels will be replaced by the New Small Wheels (NSW) [43] using small-strip TGC (sTGC) and Micro-Mesh Gaseous Structure (MicroMeGaS or Micromegas, MM for short) chambers used for both triggering and precision tracking.

At the time of the Phase-II upgrade, there will thus be no CSC chambers any more in the detector, nor will there be the Small Wheel MDT chambers, which are the ones closest to the beam line and exposed to the highest rates. Also in LS2, the BIS7 and BIS8 MDT chambers will be replaced by integrated BIS78 stations of new RPC and small diameter MDT (sMDT) chambers to enhance the trigger coverage in this region [44].

Schematic drawings of the ATLAS MS with the new detectors that will be installed in the Phase-I and Phase-II upgrades are shown in Figure 3.4.

To maintain a high trigger efficiency, new RPC chambers with increased rate capability will be installed on the inner (BI) MDT chambers of the barrel. This addresses a fundamental issue of the present (old) RPC chambers: to ensure their continued operation at the HL-LHC, these chambers will have to be operated at reduced performance (i.e. efficiency), in order to respect the original design limits on currents and integrated charge. This can be achieved by reducing the gas gain through lowering the operating voltages. In the areas of highest backgrounds, the gas gain will have to be reduced to such low levels that hit inefficiencies up to 35% will be encountered. This would reduce the trigger efficiency in the barrel region to an unacceptable level if no compensating measures were taken. In addition, due to changes in regulations, the present gas mixture used in ATLAS RPCs may need to be replaced by one with lower global-warming potential (GWP). Unless new gas mixtures are found in time, this too will imply operation of old RPCs at a reduced efficiency. Despite the lower single-hit efficiencies, a high trigger efficiency and purity can be maintained by loosening the requirements on hit coincidences in the old chambers, if at the same time a coincidence with the new BI RPC chambers is introduced. The installation of these chambers will also close most of the acceptance holes of the present barrel muon trigger, which amount to more than 20% of the  $\eta - \phi$  coverage for  $\eta < 1.05$ .

Adding new RPC chambers in the barrel is challenging in terms of available space and installation. In the small sectors, the BI RPC chambers can only be installed if the present MDT chambers are replaced by new sMDT chambers with reduced overall thickness so that the sMDT chambers and the new RPCs fit in the same envelope as the original MDT chambers. In the large sectors there is sufficient space available to add the new RPC chambers without replacing the MDTs, if on-detector services are re-arranged. The retrofitting of selected RPC chambers in the BM and BO layer in the areas of highest rate at  $\eta > 0.8$ , namely the BML7 and BOL6 chambers, is a small additional upgrade. The MDT+RPC stations will be temporarily removed from the detector to replace the

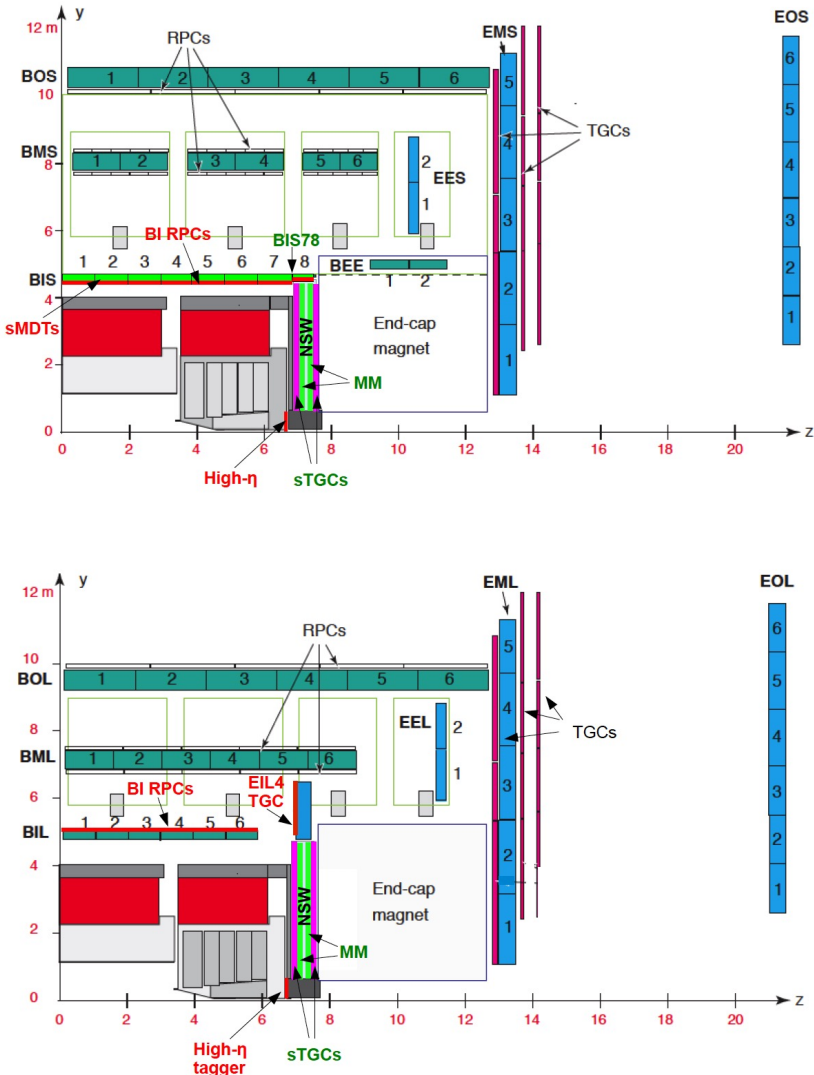


**Figure 3.4 –** Two R-Z views of the Phase-II ATLAS muon spectrometer layout showing a small sector (top) and a large sector (bottom). The drawings show the new detectors to be added in the Phase-II upgrade, including the addition of the high- $\eta$  tagger (red text: BI RPC, sMDT, EIL4 TGC, high- $\eta$  tagger), those to be installed during LS2 (green text: Micromegas and sTGC in the New Small Wheel and BIS78 RPC and sMDT), and those that will remain unchanged from the Run 1 layout (black text) [42].

front-end electronics and the readout panels, so that the chambers can be run at reduced HV without efficiency loss.

In the Section 3.4.0.1 it will be presented a study performed on the refurbish of BM and BO chambers and the installation of BI chambers in the rail sectors 11 and 15.

The retrofitting can only be done outside the experimental cavern, on the surface, since it requires the disassembly of the RPC chambers. The retrofitting of the BO chambers does not fit into the LS3 schedule because it would interfere with the BI chamber upgrade, and will likely be performed, at least partly, in winter shutdowns after LS3.

The main limitations of the RPC system for operation at the HL-LHC are related to the chambers, owing to the more than a factor of seven higher luminosity than the chambers were designed for. The RPC rate capability depends on the total charge delivered per count, which, for the present RPCs, is 30 pC.

As a consequence, the single-gap efficiency will have to be reduced on average by 15%, and by 35% at large  $\eta$ . This efficiency loss will be compensated by installing a new layer of trigger chambers in the BI layer, increasing the overall barrel trigger redundancy.

To operate reliably at the HL-LHC, with high acceptance and efficiency and maintaining, the high trigger selectivity of the present system, several upgrades are required for the RPC system:

- A new inner layer of BI RPC chambers will be added to the spectrometer. This will recover most of the current geometrical acceptance holes. The redundancy of the system will be greatly enhanced, so that full trigger efficiency can be maintained even if the old RPCs have to be operated at reduced efficiency, either to limit the effects of ageing or because the use of a different gas mixture is enforced. The BI RPCs will be new-generation RPCs with 1 mm gas gaps and high-sensitivity front-end electronics.
- The trigger and readout electronics (Pad and splitter boxes) have to be replaced in order to make the RPC system compliant with the Phase-II ATLAS trigger and readout scheme. The entire electronics chain, except for the front-end boards, will be replaced. The Pads will be replaced by the new data collector and transmitter (DCT) boards that will send all data off the detector to the counting room USA15 where the trigger and readout logic will be performed.
- In a worst-case scenario for the required reduction of efficiency of the old RPCs, a reduction of the trigger efficiency may still occur even after the BI RPC installation, in the region of  $|\eta| > 0.8$ . This efficiency loss can be recovered by retrofitting a limited number of BO chambers in that region. The retrofitting comprises replacing the original front-end electronics by the new BI version, and replacing the readout strip panels.

### 3.2.1 RPC upgrade

The BI system is designed to increase the trigger acceptance and the trigger efficiency, by loosening the requirements on the number of hits in the BM and BO chambers and, at the same time, adding the requirement of a coincidence with the BI layer. Any coincidences of hits in at least three chambers out of four (counting one BI, two BM, and one BO) will be accepted. Two-chamber BI-BO coincidences will be used to cover the remaining acceptance holes. Details of the Phase-II trigger algorithms and their performance are discussed in Section 3.3. Figure 3.5 illustrates the recovery of acceptance and efficiency obtained with the Phase-II trigger including the BI RPCs in a worst-case scenario in which the single-hit efficiency of the old RPC is reduced by 15–35% as a function of  $|\eta|$ , depending on the rate to which each chamber is exposed.

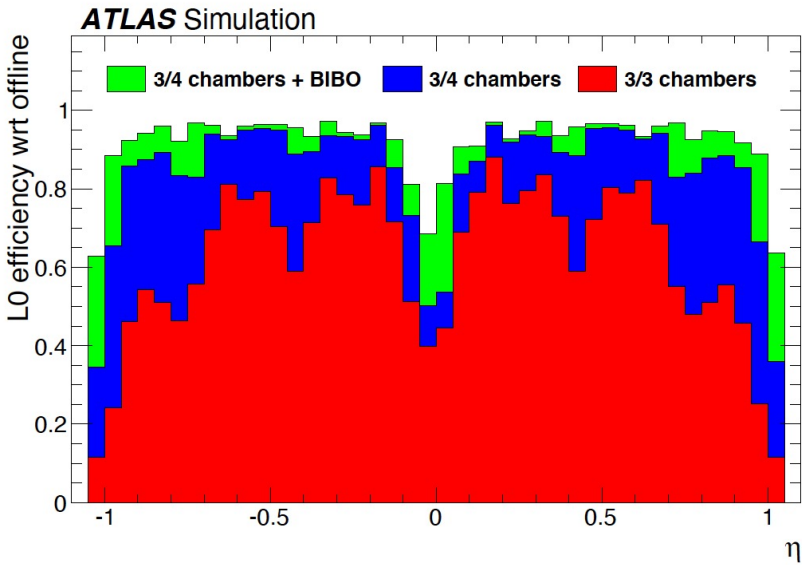


**Figure 3.5** – Efficiency times acceptance of the L0 barrel trigger for reconstructed muons with  $p_T = 25$  GeV as a function of  $\eta$ , assuming the worst-case scenario [42].

The new BI RPC chambers will have three sensitive gas gaps that are read out independently. A majority logic requiring hits in at least two out of three planes provides high efficiency while suppressing the rate of random coincidences due to uncorrelated hits from photons and neutrons. This is necessary, for instance, to keep the rate of BI-BO coincidences at an acceptable level.

A major re-design of the RPC technology started around the year 2010, mainly aiming at a better rate capability and ageing behaviour. The new design is based on a reduced thickness of the gas gaps (from 2 mm to 1 mm) and of the resistive electrodes (from 1.8

mm to 1 mm), and on the use of a new generation of low-noise high-sensitivity amplifiers. Using these amplifiers, full efficiency can be achieved for a lower voltage across the gas gap, thus transferring part of the amplification from the gas avalanche to the electronics. In this way, the RPCs can be operated at a reduced charge per avalanche, reducing the detector current and thus improving rate capability and ageing.

A detail view of the positions of the BI RPCs in ATLAS is shown in Figure 3.6.

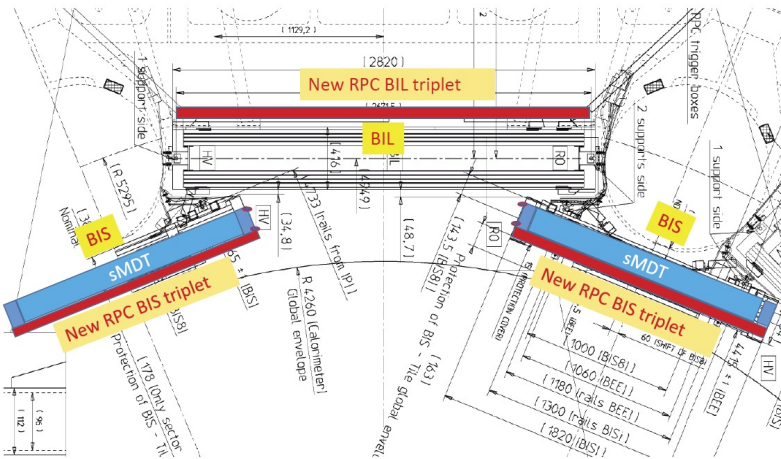


**Figure 3.6** – X-Y view of the inner barrel layer, indicating the positions of the BI RPCs (red) and BIS sMDTs (blue) in the small and large sectors [42].

In the small sectors (BIS), due to the tight space limitations, the MDT chambers need to be replaced by new small-diameter MDT (sMDT) chambers with half the tube diameter (15 mm instead of 30 mm) in order to create space for the RPCs on the inside of the sMDT chambers. In the large sectors (BIL), the new RPCs will be installed on the outside of the existing MDTs. The layout of the new BI RPCs leaves the necessary holes and cut-outs for the existing MDT alignment lines and for detector services. It comprises 272 triplet RPC chambers, for a total area of about 470 m<sup>2</sup>. Acceptance studies based on a realistic description of the BI RPC geometry show a geometrical acceptance of the BI RPC chambers of 91% for reconstructed muons with  $|\eta| < 1.05$ , compared to 95% for the MDT chambers. This results in a barrel trigger acceptance of 96%.

Each detector layer of the triplets is read out on both surfaces by orthogonal strip panels, providing  $\eta$  and  $\phi$  measurements. The compact triplet structure and the use of highly sensitive amplifiers require a complete isolation of individual layers from each other. The choice of strip pitches, 24–26 mm depending on the chamber type, has been constrained by the performance requirements, the strip impedance, and cost considerations. The total number of readout channels is about 8700.

### 3.2.2 Trigger scheme

All the hits from RPC detectors will be available to the barrel Sector Logic board that uses them to generate barrel trigger candidates. The new BI RPCs increase the geometrical acceptance of the present barrel muon trigger and its robustness against inefficiencies of the old BM and BO RPCs caused by the reduced operating voltages necessary to ensure their longevity.

The RPC trigger will use nine measurement planes, provided by four layers of RPC chambers: one BI triplet (RPC0), two BM doublets (RPC1 and RPC2), and one BO doublet (RPC3). Figure 3.7 shows the positions of the BI, BM, and BO RPC chambers in a small barrel sector together with the MDT chambers. The acceptance holes in the BM layer, caused by the magnet coils and their supports, are also visible.

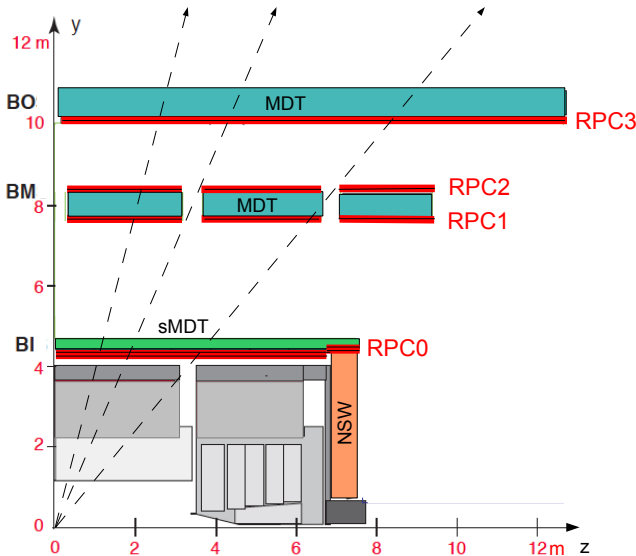


**Figure 3.7 –** Transverse section of a small sector in the barrel region, showing the four layers of RPC chambers (RPC0,1,2,3), as well as the MDT chambers in the barrel-inner (BI), barrel-middle (BM), and barrel-outer (BO) layers. The three dashed lines represent muon trajectories traversing four, two, and three RPC chambers [42].

To take advantage of the redundancy of detector planes, a trigger algorithm that does not make use of a fixed pivot plane (as in present ATLAS muon trigger) has been developed. This makes it possible to define different trigger coincidence logic schemes.

These schemes (summarized in Table 3.1) are based on different requirements on the four layers of RPC chambers:

- 3/3 chambers. Hits in at least three out of four planes of the RPC1+RPC2 chambers and in at least one out of two planes of RPC3. This is equivalent to the present high-pT trigger.
- 3/4 chambers. The previous requirement in a logical OR with the requirement of hits in at least two planes out of three in RPC0 and in at least three planes out of six in RPC1+RPC2+RPC3. In this way, all combinations of three-chamber coincidences (satisfying the above hit requirements) are accepted.
- 3/4 chambers + BI-BO. The previous requirement in a logical OR with the requirement of at least two hits in RPC0 and at least one hit in RPC3. This enhances the trigger coverage in the regions where no BM RPCs are installed due to the mechanical support structure of the toroid coils. The BI-BO coincidence is expected to be prone to accidental coincidences of uncorrelated background hits that are negligible in three-chamber coincidences. In the baseline version of this trigger, BI-BO coincidences are used in the whole barrel region, but can be limited to the BM acceptance gaps, if the muon trigger rate in the barrel gets too high.

Trigger	Requirement
3/3 chambers	$3[\text{RPC1+RPC2}] \text{ AND } 1[\text{RPC3}]$
3/4 chambers	$(3[\text{RPC1+RPC2}] \text{ AND } 1[\text{RPC3}]) \text{ OR } (2[\text{RPC0}] \text{ AND } 3[\text{RPC1+RPC2+RPC3}])$
3/4 ch.+BI-BO	$(3[\text{RPC1+RPC2}] \text{ AND } 1[\text{RPC3}]) \text{ OR } (2[\text{RPC0}] \text{ AND } 3[\text{RPC1+RPC2+RPC3}])$ $\text{OR } (2[\text{RPC0}] \text{ AND } 1[\text{RPC3}])$

**Table 3.1** – The hit requirements used in different RPC triggers. The left column shows the short name used in the text. The right column gives the coincidence scheme used for the selection logic. The notation  $N[\text{RPC}_i+\text{RPC}_j+\dots]$  indicates a majority requirement of hits in at least  $N$  planes out of all the possible planes available in RPC chambers  $\text{RPC}_i$ ,  $\text{RPC}_j, \dots$  with  $i, j, \dots \in \{0, 1, 2, 3\}$ .

### 3.3 Hit digitization in the BI region

Since at the present time the new chambers in the BI region are not yet installed, the simulation performed for this work takes into account the presence of hits in the BI RPC chambers exploiting the true hits, recorded by the MDT chambers in the BI region, and treating them as hits of the future RPC chambers.

In this work, it has been used the common framework `muTrigNt_write` [45] that includes a realistic digitization. This code reproduces the dimensions of the new BI RPC chambers and, given as input the true MDT hits, it checks if the hits are in the geometric acceptance.

The code allows to generate strips (both in  $\eta$  and  $\phi$  coordinates) as well and thus to digitize the true MDT hit recording its as a hit in the middle of the strip. This `muTrigNt_write` is also able to simulate the trigger efficiencies as described in Sec 3.4. They have been calculated considering muons reconstructed in  $\eta < 1.05$  by the offline reconstruction, using a single-muon Monte Carlo sample with fixed  $p_T = 50$  GeV and uniform distributions in  $\eta$  and  $\phi$ . It is the official Muon-phase2 sample `mc15_14TeV.422063.ParticleGun_single_mu_Pt50.recon.ESD.e5392_s2988_s3000_r8974` [46], containing 50K events, produced with the ITk (Inner Traker) simulation and with the layout of Run-I muons, that differs compared to the layout of Run-II muons because the feet and the elevator chambers are missing. The simulation implements a more realistic digitization that produces:

- cluster size, strip number and the associated coordinates of the strips (Section 3.3.1);
- timing (Section 3.3.2);
- the option of BI RPCs with two-sides  $\eta - \eta$  readout (Section 3.3.3);
- BI and BMBO Efficiencies (Section 3.4);

### 3.3.1 The cluster size model

A single discharge in the gas volume can induce a signal in more than one RPC strip (i.e. occurs a so-called *cluster*), this is due to the charge sharing.. The number of RPC strips fired in temporal coincidence is called *cluster size*. The cluster size is a relevant parameter for RPC detector and it must be strictly monitored to ensure a full trigger efficiency, The cluster size is simulated using a Gaussian charge distribution, with fixed width and centered on the true MDT hit that is induced on the strips [47]. This function is defined as:

$$G(z) = f(A) \cdot \text{erf} \left( \frac{\mu - z}{\sigma \sqrt{2}} \right) \quad (3.1)$$

where the amplitude distribution  $f(A)$  is variable with an exponential decreasing tail  $f(A) = e^{-\frac{A}{\tau}}$ , with the parameters  $\tau = 0.8$  and random  $A$ , fixed width  $\sigma = 16$  mm and  $\mu$  is the  $z$  - coordinate of the hit.

When the charge integrated over a strip exceeds a certain threshold (0.2 in this simulation), then the strip is switched on.

This is not a strictly physical model but a decreasing exponential is useful to produce the expected tail, unless to use a more realistic model for amplitudes based on experimental studies. A picture of the model used in this simulation is illustrated in Figure 3.8. Cluster size is given by the number of strips fired at the same time. It depends on the absolute value of charge integrated over a strip but it also depends on the the position of the true hit.

Originally, the RPC hit is fixed to be at the center of the strip and the true MDT hit belongs to one strip only but in this simulation, it would be possible to have many strips

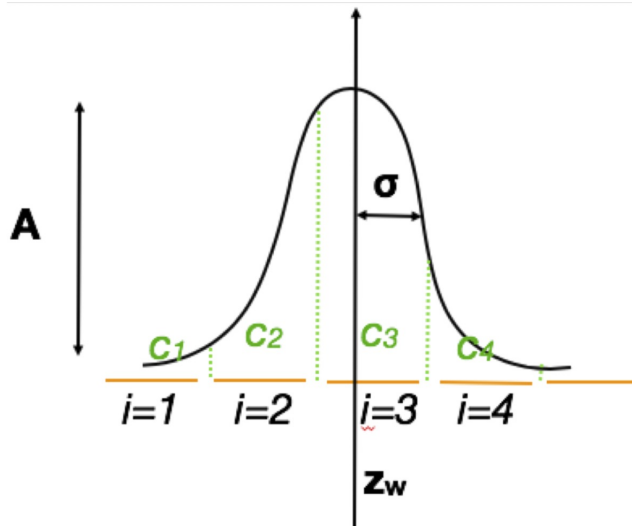


**Figure 3.8** – Cluster size model used in the simulation.  $C_i$  is the charge integrated over a strip  $i$ . Some other parameters are the strip pitch  $z_w$  ( 22 mm), random amplitude  $A$  and width  $\sigma$ . When the charge integrated over a strip exceeds a certain threshold, the strip is switched on [47].

fired at the same time using the relation:  $\text{GlobPos}_i = \text{GlobPos}_{i,\text{true}} \pm \text{strip\_center}_i$ . The resulting cluster size distribution is shown in Figure 3.9.

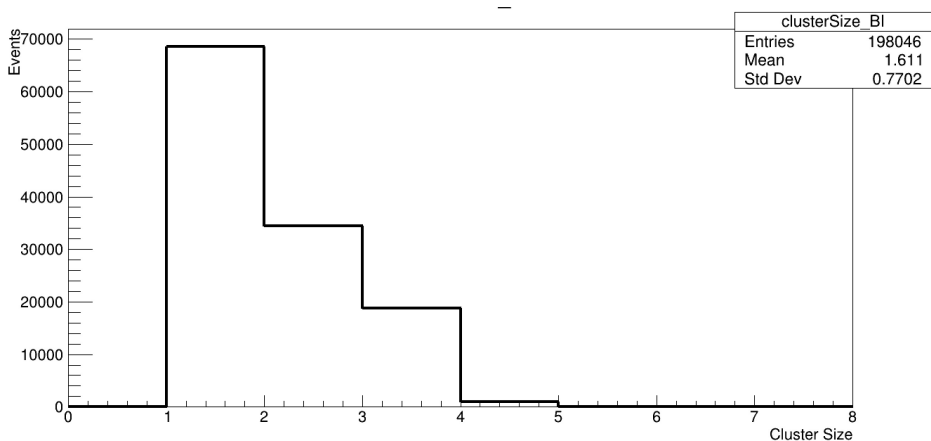


**Figure 3.9** – Cluster size distribution obtained with the model and parameters illustrated in this section. The average value is 1.6.

Looking at the hit distribution in Figure 3.10(a) for the  $\eta$  layer and Figure 3.10(b) for the  $\phi$  layer, it is possible to see that:

- CS=0 never possible by definition, one hit corresponds at least at one fired strip;
- CS=1 the hit distribution is uniform, because the integrated charge is less than the fixed threshold;
- CS=2 mostly when the truth hit is far from the strip center and at the strip edge;
- CS=3 mostly when the truth hit is far from the strip edge and at the strip center;
- CS>3 are rare events but they follow the same pattern.

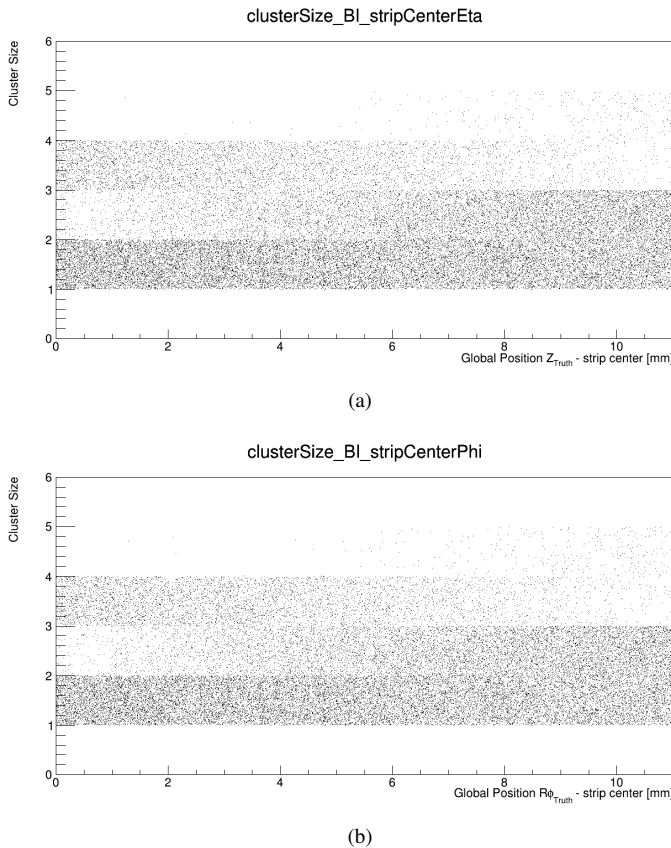


**Figure 3.10 –** RPC hit distribution GlobPos<sub>i</sub> for a) strips along  $\eta$  and b) strips along  $R\phi$ .

Strips in  $\eta$  and  $\phi$  layers are orthogonal to each other and it is possible to see how they are arranged as a function of the Global Position in the BI region of the ATLAS detector. In particular, in Figure 3.11(a) strips oriented along  $\eta$  are ordered in such a way that the strip number one is the inner strip, while Figure 3.11(b) shows that strips oriented along  $\phi$  are always oriented with increasing  $\phi$ .

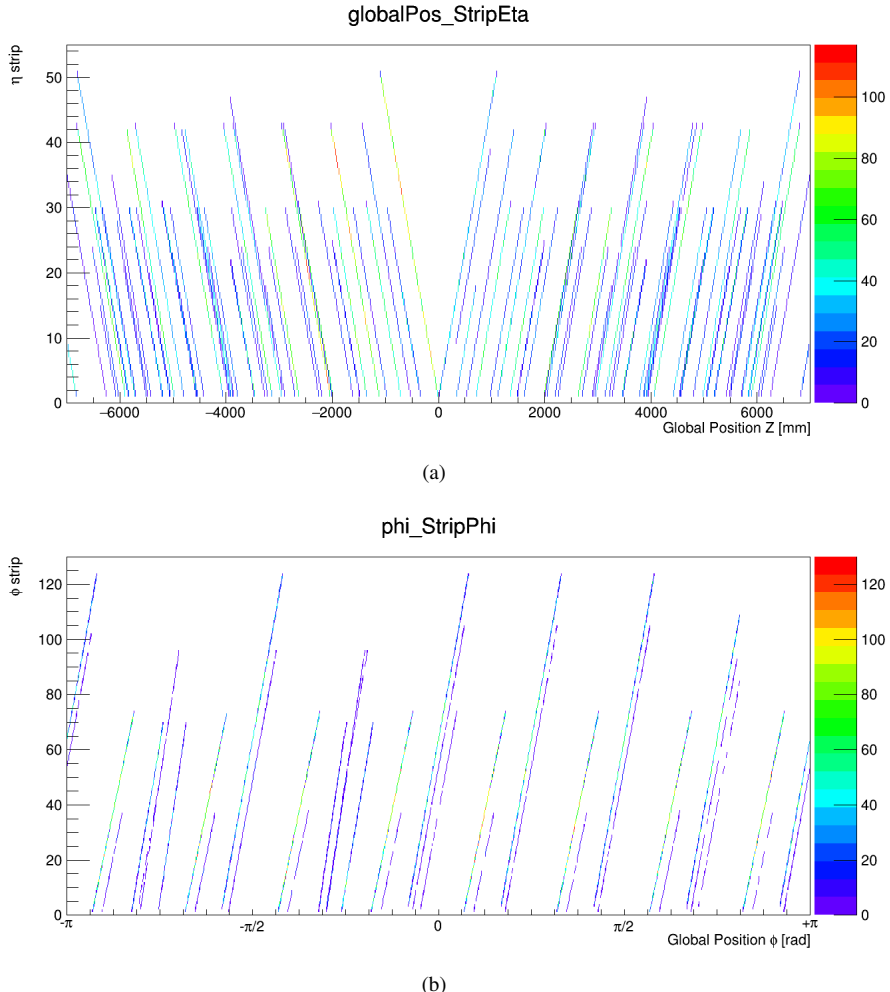


**Figure 3.11** – Arrangement of strips in the a)  $\eta$  layer and b)  $\phi$  layer as a function of the Global Position in the BI region of the ATLAS detector.

Figure 3.12 summarize the main chamber parameters of the expected layout for the Phase II upgrade. Strip and front-end board entries are based on the assumptions of a 20 mm pitch and eight channels per board.

Figure 3.13 shows the number of  $\eta$  and  $\phi$  strips switched on in the simulation. It is possible to verify that the simulation developed for this work follows the requirements of the Phase II upgrade for BI RPCs to be realistic and reliable as much as possible.

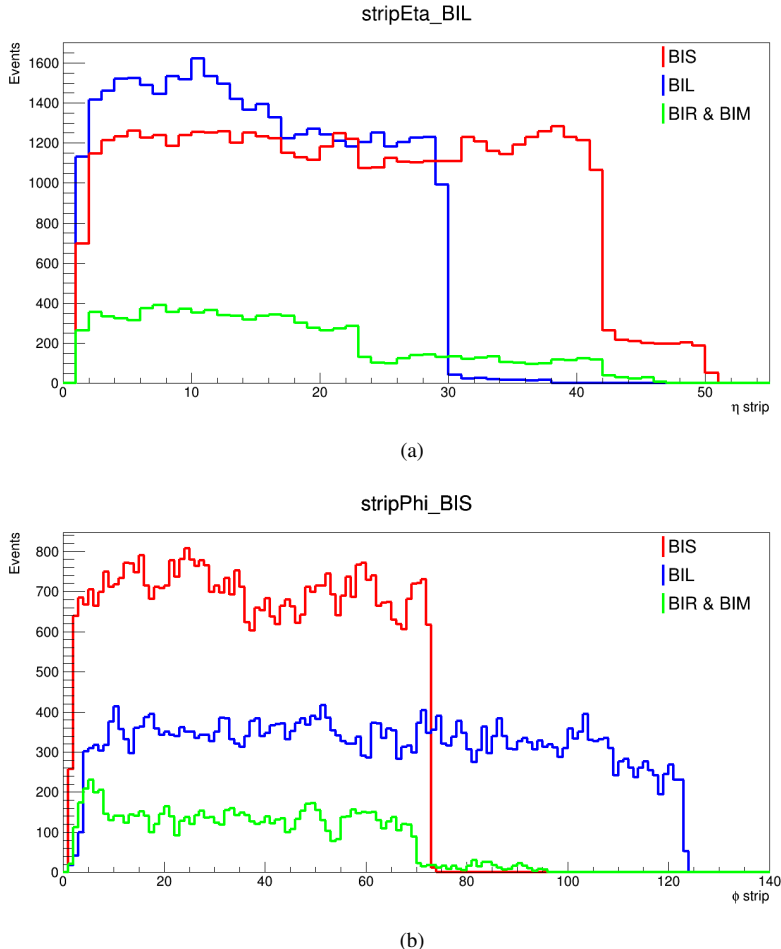
RPC type	BIL-A	BIL-B	BIL-C	BIL-D	BIL-K	BIL-E	BIL-F	BIL-G	BIL-H	BIL-I	BIL-J
# of units	72	2	4	2	2	14	2	8	6	2	2
# of layers	3	3	3	3	3	3	3	3	3	3	3
length in Z (mm)	640	510	365	600	220	640	540	450	310	370	370
width in $\phi$ (mm)	2750	2750	2750	2750	2750	2380	2380	2300	2100	1850	1700
$\eta$ strip pitch (mm)	18.4	19.2	19.7	17.2	21.3	18.4	20.4	16.7	16.3	20.0	20.0
$\phi$ strip pitch (mm)	21.1	21.1	21.1	21.1	21.1	20.8	20.8	21.6	21.4	20.5	20.6
# $\eta$ strips/layer	32	32	16	32	8	32	24	24	16	16	16
# $\eta$ strips/unit	96	96	48	96	24	96	72	72	48	48	48
# $\phi$ strips/layer	128	128	128	128	128	112	112	104	96	88	80
# $\phi$ strips/unit	408	408	408	408	408	360	360	336	312	288	264
area/layer ( $m^2$ )	1.76	1.40	1.00	1.65	0.61	1.52	1.29	1.04	0.65	0.68	0.63
gap area ( $m^2$ )	1.61	1.25	0.86	1.50	0.47	1.39	1.15	0.91	0.54	0.58	0.54
Gas volume/layer (l)	4.82	3.76	2.59	4.49	1.41	4.16	3.46	2.73	1.63	1.75	1.61
# FE cards/layer $\eta$	4	4	2	4	1	4	3	3	2	2	2
# FE cards/layer $\phi$	16	16	16	16	16	14	14	13	12	11	10

(a)

RPC type	BIR-A	BIR-B	BIR-C	BIR-D	BIM-A	BIM-B	BIS-A	BIS-B
# of units	4	8	8	4	12	24	16	80
# of layers	3	3	3	3	3	3	3	3
length in Z (mm)	780	916	1104	735	437	495	1096	916
width in $\phi$ (mm)	2099	1251	819	1260	1536	1536	1820	1820
$\eta$ strip pitch (mm)	18.3/22.8	21.7	22.0	21.4	16.1/24.2	18.5/27.8	21.8	21.7
$\phi$ strip pitch (mm)	21.3	21.4	19.2/24.0	21.6	20.6	20.6	20.1	20.1
# $\eta$ strips/layer	40/32	40	48	32	24/16	24/16	48	40
# $\eta$ strips/unit	120/96	144	168	96	72	72	168	120
# $\phi$ strips/layer	96	56	40/32	56	72	72	88	88
# $\phi$ strips/unit	288	168	120/96	168	216	216	264	264
area/layer ( $m^2$ )	1.64	1.15	0.90	0.93	0.67	0.76	2.00	1.67
gap area ( $m^2$ )	1.51	1.05	0.82	0.84	0.58	0.67	1.86	1.54
Gas volume/layer (l)	4.52	3.15	2.45	2.51	1.75	2.01	5.59	4.63
# FE cards/layer $\eta$	5/4	5	6	4	3/2	3/2	6	5
# FE cards/layer $\phi$	12	8	5/4	7	9	9	11	11

(b)

**Figure 3.12 – Main parameters of a) the BIL RPC chambers and b) the BIR/BIM/BIS RPC chambers [42].**

**Figure 3.13**

### 3.3.2 Timing

Another important variable is the time taken for the particle to pass through the detector. It is important because it is one of the discriminating variables in the algorithm's selection of hits. Hits recorded in the bunch crossing event are considered and not all the hits previously recorded. Therefore, all hits outside 25 ns coincidence window around the bunch crossing of interest are excluded.

In order to simulate the new RPCs one has to take into account several effects and apply an appropriate correction and extract a digital readout.

The final formula used to extract digitized time in which the hit is recorded by the detector is:

$$t_{hit} = \text{int}^1 \left( \frac{t_{true} + t_{Gauss} + t_{FE} - t_{cal}}{\Delta t} \right) \Delta t \quad (3.2)$$

- $t_{true}$  is the true hit recorded by the MDT;
- $\Delta t$  is the sampling rate (0.3 ns). The final  $t_{hit}$  must be a multiple of the sampling rate to have a digitization;
- $t_{Gauss}$  is a Gaussian term that reproduces the fluctuations in the RPC signal (smearing 0.4 ns);
- $t_{FE}$  is the propagation of the signal along the strip to the FE electronics assuming that the signal speed on the layer is 200 mm/ns;
- $t_{cal}$  is the calibration offset. The true hit timing is recorded referring to the time of the collision on the MDT tubes. To report the timing centered around 0, it was necessary to subtract the time of flight of the particle assuming time to be calibrated with prompt muons crossing the center of the strip at  $t = 0$ .

Figure 3.14 shows the digitized time associated to the RPC hit calculated using the Equation 3.2. The tail of the distribution is given by low  $p_T$  muons that produce secondary hits.

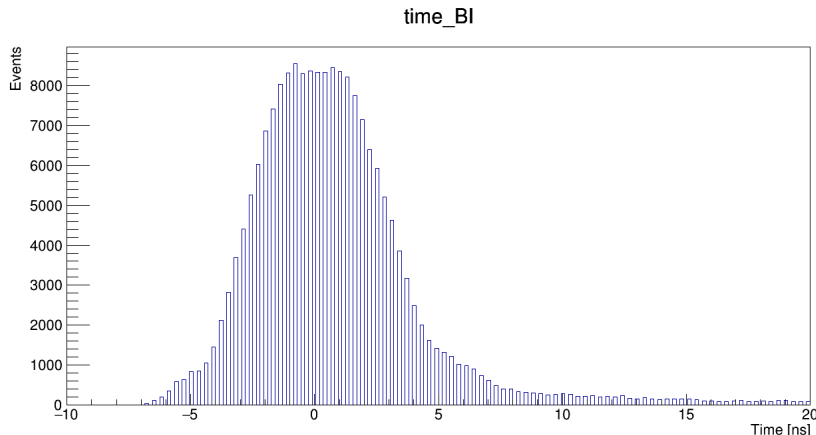


**Figure 3.14 –** Digitized time associated to the RPC hit. The tail of the distribution is given by low  $p_T$  muons that produce secondary hits

---

<sup>1</sup>The  $\text{int}$  function takes the integer part of a natural number.

### 3.3.3 BI RPCs with two-sides $\eta - \eta$ readout

## 3.4 L0 barrel trigger efficiency

The performance of the barrel muon trigger was studied for a fixed transverse momentum threshold:  $p_T > 10$  GeV [48]. To study the robustness of the trigger against possible efficiency reductions of the old RPCs in the BM and BO layers, the simulation was performed in the so-called "worst-case-scenario" that introduces inefficiencies depending on the station type and sector and summarized in Table 3.2. This scenario include inefficiencies due to a reduction of the high voltage of the BM and BO RPCs such that the expected RPC current is always below the safe operation limit.

Station Name	StationEta							
	1	2	3	4	5	6	7	8
BOL	0.90	0.90	0.82	0.82	0.76	0.74	-	-
BOS/BOG/BOF	0.89	0.90	0.90	0.90	0.89	0.66	0.60	0.60
BML	0.88	0.88	0.88	0.83	0.56	0.56	0.60	-
BMS	0.90	0.90	0.90	0.87	0.81	0.81	-	-

**Table 3.2** – Efficiency for each station and sector of the barrel muon trigger in the "worst-case-scenario". This scenario includes inefficiencies due to a reduction of the HV of the BM and BO RPC [48]..

The trigger efficiency times acceptance is defined as the fraction of reconstructed muons that are accepted by the trigger, using the simulation that includes the RPC detector efficiency. Starting from the WCS scenario, several other cases were studied in order to understand what would be the impact of retrofitting some chambers with new electronics.

### 3.4.0.1 BM and BO retrofitting

In the first case presented, efficiencies of the "worst-case-scenario" are used except for the following stations, setted to 100% efficiency:

1. BML 7,
2. BOL 6,
3. BOS 6,
4. BOL 5.

The products of muon trigger efficiency and acceptance for the BM and BO retrofitting are listed in Table 3.3.

The trigger efficiency times acceptance is also presented in Figure 3.15 that compare the "worst-case scenario" with all the variants of the WCSe, in which some stations are fixed to 100% efficiency.

BM and BO efficiency (%)	Trigger efficiency x acceptance (%)		
	3/3 chambers	3/4 chambers	3/4 chambers + BIBO
WCS	58.78	83.27	91.89
Case 1a (BML 7 100%)	+0.22	+0.26	+0.14
Case 1b (BOL 6 100%)	+0.13	+1.08	+0.53
Case 1c (BOS 6 100%)	+0.16	+0.51	+0.63
Case 1d (BOL 5 100%)	+0.23	+0.82	+0.41

**Table 3.3** – Efficiency times acceptance for the L0 barrel trigger for different assumptions on the hit efficiency of the present RPC detectors. The “WCS” row corresponds to the scenario in which the efficiencies are listed in Table 3.2. The other rows correspond to the variants of the WCS, in which the efficiency of some stations are setted to 100%. The correspondent results of these variants, are expressed as variations to the WCS [48]..

### 3.4.0.2 Dropping BIR and BIM chambers

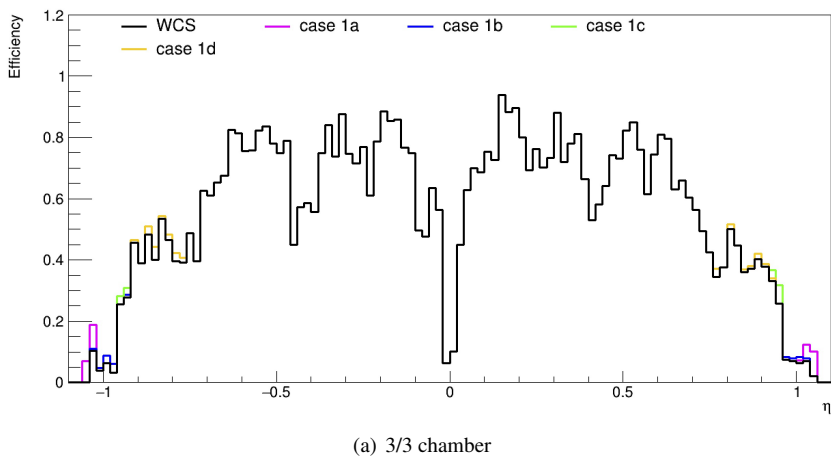
Since the installation of the RPCs in the sectors 11 and 15 (BIM and BIR) seems to be very hard, another special case was performed simulating a scenario in which BI RPC are not installed in these sectors.

The products of muon trigger efficiency and acceptance for the second case are listed in Table 3.4.

The results are also presented in Figure 3.16(c) that compares the "worst-case scenario" with this second case, in which BIM and BIR are turned off.

BM and BO efficiency (%)	Trigger efficiency x acceptance (%)		
	3/3 chambers	3/4 chambers	3/4 chambers + BIBO
WCS	58.78	83.27	91.89
Case 2 (BIM BIR off)	+0.03	-2.70	-3.11

**Table 3.4** – Efficiency times acceptance for the L0 barrel trigger for different assumptions on the hit efficiency of the present RPC detectors. The WCS row corresponds to the scenario in which the efficiencies are listed in Table 3.2. The row "Case 2" corresponds to the case in which RPCs in the sectors 11-15 (BIM and BIR) are turned off. The correspondent results of the Case 2, are expressed as variations to the WCS [48].



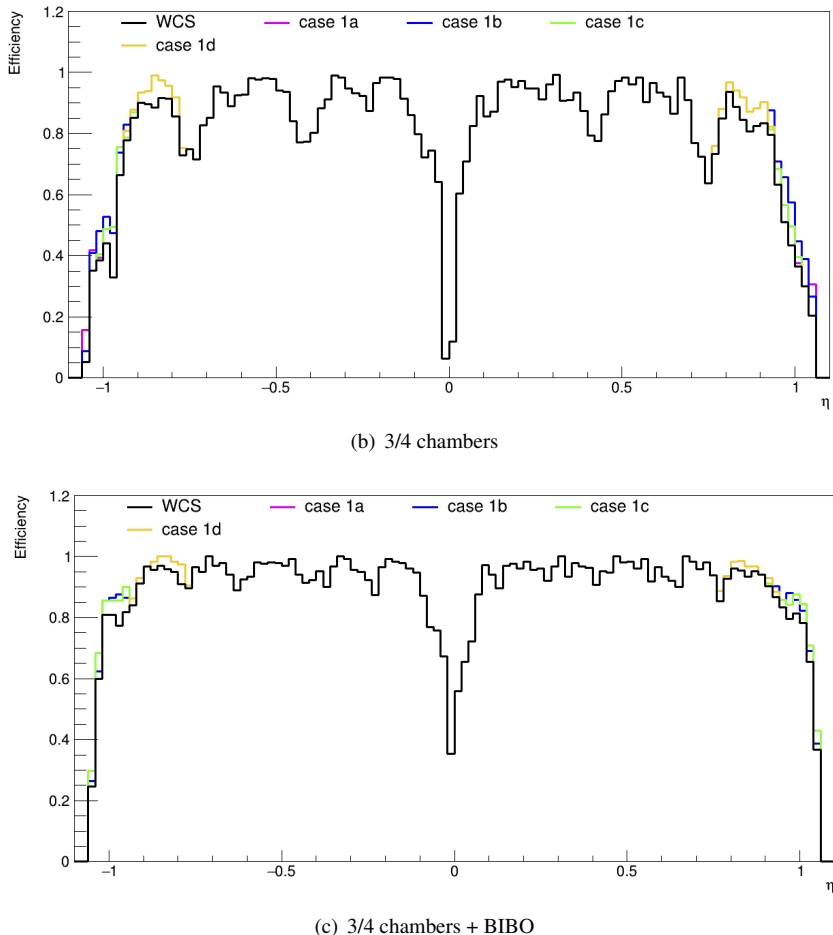
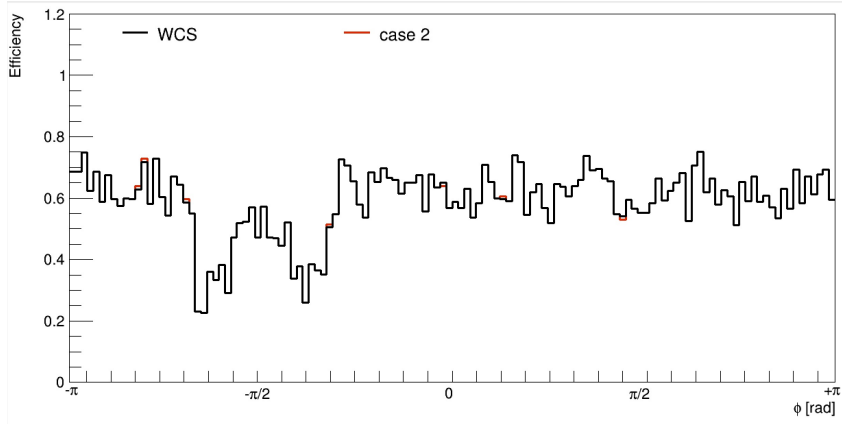


**Figure 3.15** – Efficiency times acceptance of the L0 barrel trigger compared to reconstructed muons with  $p_T = 50$  GeV as a function of  $\eta$  taking in to account all the variants of the WCS. The histograms show the efficiency of the existing 3/3 chambers trigger, of the 3/4 chambers trigger including the BI layer, and the additional gain from the BI-BO trigger. Efficiency times acceptance is defined as the fraction of reconstructed muons accepted by the trigger, using a simulation that includes the RPC detector efficiency [48].



(a) 3/3 chambers

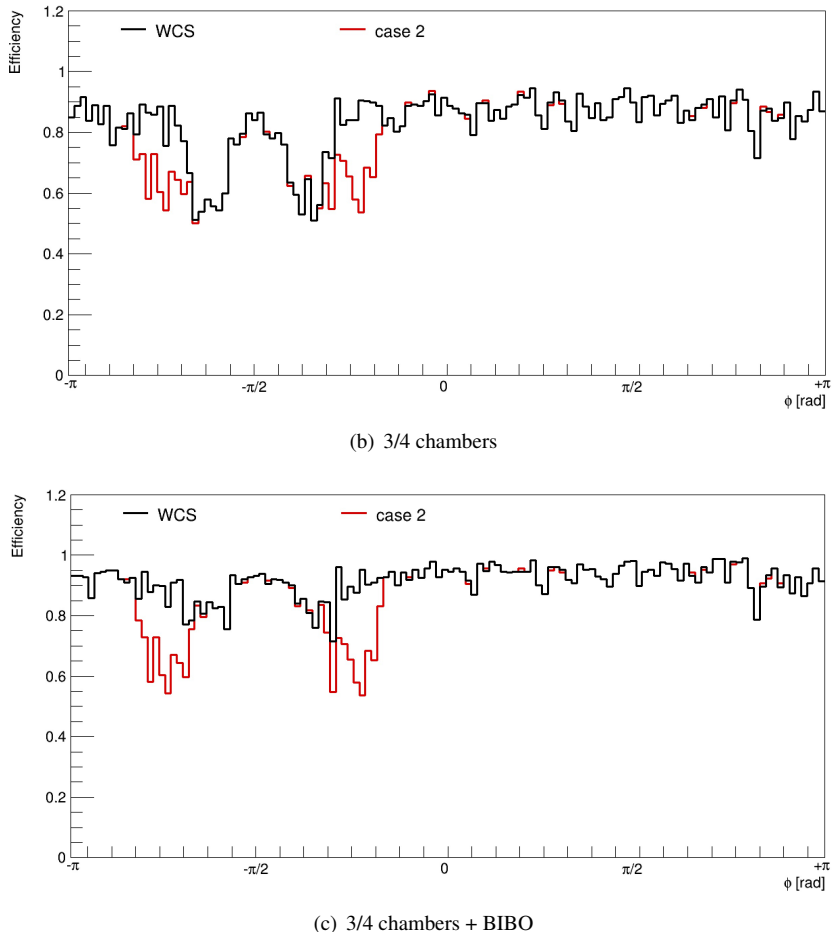


**Figure 3.16** – Efficiency times acceptance of the L0 barrel trigger compared to reconstructed muons with  $p_T = 50$  GeV as a function of  $\phi$ . The histograms show the efficiency of the existing 3/3 chambers trigger, of the 3/4 chambers trigger including the BI layer, and the additional gain from the BI-BO trigger. Efficiency times acceptance is defined as the fraction of reconstructed muons accepted by the trigger, using a simulation that includes the RPC detector efficiency [48].

# CHAPTER 4

---

## The Soft Muon Tagging

---

## 4.1 The soft muons

## 4.2 Working Point definition

## 4.3 Mistag rate measurement

## 4.4 Efficiency measurements

# CHAPTER 5

---

Search for the FCNC decay of top-quark in c-quark  
and Z boson

---

## 5.1 Physics motivation

## 5.2 Analysis strategy

### 5.3 MC simulated samples

## 5.4 Event selections and reconstruction

$$\chi^2 = \frac{(m_{j_{SM} l_a l_b}^{reco} - m_{t_{FCNC}})^2}{\sigma_{t_{FCNC}}^2} + \frac{(m_{j_{bjet} l_c \nu}^{reco} - m_{t_{SM}})^2}{\sigma_{t_{SM}}^2} + \frac{(m_{l_c \nu}^{reco} - m_W)^2}{\sigma_W^2} \quad (5.1)$$

### 5.4.1 Offline selection

### 5.4.2 Event classification

### 5.4.3 Background control and validation regions

## 5.5 Estimation of the fake-lepton background

### **5.5.1 Fake Scale Factors fit regions**

### **5.5.2 Determination of Fake Scale Factors**

## 5.6 Signal-to-background discrimination

## 5.7 Background estimation

### 5.7.1 Signal injection tests

## 5.8 Systematic uncertainties

## 5.9 Statistical analysis

## 5.10 Results

# CHAPTER 6

---

## Conclusions

---

# APPENDIX A

---

## Mass Resolution

---

---

## References

---

- [1] E. Fermi, *Il Nuovo Cimento* (1934) **11**, 1 (2008).
- [2] F. L. Wilson, *Am.J.Phys* **36**, 1150 (1968).
- [3] C. S. Wu, E. Ambler, R. W. Hayward, D. D. Hoppes, and R. P. Hudson, *Phys. Rev.* **105**, 1413 (1957).
- [4] P. Renton, *Electroweak Interactions: An Introduction to the Physics of Quarks and Leptons* (1990).
- [5] S. L. Glashow, J. Iliopoulos, and L. Maiani, *Phys. Rev. D* **2**, 1285 (1970).
- [6] J. Aguilar-Saavedra, “Top flavour-changing neutral interactions: theoretical expectations and experimental detection,” (2004), arXiv:hep-ph/0409342 [hep-ph] .
- [7] N. Cabibbo, *Meeting of the Italian School of Physics and Weak Interactions Bologna, Italy, April 26-28, 1984*, *Phys. Rev. Lett.* **10**, 531 (1963).
- [8] M. Kobayashi and T. Maskawa, *Progress of Theoretical Physics* **49**, 652 (1973).
- [9] Z. Ligeti, *Int. J. Mod. Phys.* **A20**, 5105 (2005), arXiv:hep-ph/0408267 [hep-ph] .
- [10] F. Abe *et al.* (CDF Collaboration), *Phys. Rev. Lett.* **74**, 2626 (1995).
- [11] S. Abachi *et al.* (D0 Collaboration), *Phys. Rev. Lett.* **74**, 2632 (1995).
- [12] R. Aaij *et al.* (LHCb Collaboration), *Phys. Rev. Lett.* **115**, 112001 (2015).
- [13] M. Tanabashi *et al.* (Particle Data Group), *Phys. Rev. D* **98**, 030001 (2018).
- [14] W. Bernreuther, *J. Phys.* **G35**, 083001 (2008), arXiv:0805.1333 [hep-ph] .

- [15] D0 Collaboration website, “Useful Diagrams of Top Signals and Backgrounds,” .
- [16] G. Aad *et al.* (ATLAS), *Phys. Lett.* **B716**, 1 (2012), arXiv:1207.7214 [hep-ex] .
- [17] F. Zwicky, *General Relativity and Gravitation* **41**, 207 (2009).
- [18] N. Aghanim *et al.* (Planck), (2018), arXiv:1807.06209 [astro-ph.CO] .
- [19] J. A. Aguilar-Saavedra, *Acta Phys. Polon.* **B35**, 2695 (2004), arXiv:hep-ph/0409342 [hep-ph] .
- [20] J. A. Aguilar-Saavedra, *Phys. Rev.* **D67**, 035003 (2003), arXiv:hep-ph/0210112 [hep-ph] .
- [21] D. Atwood, L. Reina, and A. Soni, *Phys. Rev. D* **55**, 3156 (1997).
- [22] J. J. Cao, G. Eilam, M. Frank, K. Hikasa, G. L. Liu, I. Turan, and J. M. Yang, *Phys. Rev. D* **75**, 075021 (2007).
- [23] J. M. Yang, B.-L. Young, and X. Zhang, *Phys. Rev. D* **58**, 055001 (1998).
- [24] K. Agashe, G. Perez, and A. Soni, *Phys. Rev. D* **75**, 015002 (2007).
- [25] P. Hung, Y.-X. Lin, C. S. Nugroho, and T.-C. Yuan, *Nuclear Physics B* **927**, 166 (2018).
- [26] K. Agashe *et al.* (Top Quark Working Group) (2013) arXiv:1311.2028 [hep-ph] .
- [27] S. L. Glashow and S. Weinberg, *Phys. Rev. D* **15**, 1958 (1977).
- [28] E. A. Paschos, *Phys. Rev. D* **15**, 1966 (1977).
- [29] V. D. Barger, M. S. Berger, and R. J. N. Phillips, *Phys. Rev. D* **52**, 1663 (1995), arXiv:hep-ph/9503204 [hep-ph] .
- [30] Z. Maki, M. Nakagawa, and S. Sakata, *Prog. Theor. Phys.* **28**, 870 (1962).
- [31] G. C. Branco, P. M. Ferreira, L. Lavoura, M. N. Rebelo, M. Sher, and J. P. Silva, *Phys. Rept.* **516**, 1 (2012), arXiv:1106.0034 [hep-ph] .
- [32] G. Couture, C. Hamzaoui, and H. König, *Phys. Rev. D* **52**, 1713 (1995).
- [33] L. Evans and P. Bryant, *Journal of Instrumentation* **3**, S08001 (2008).
- [34] E. Mobs, “The CERN accelerator complex - August 2018. Complexe des accélérateurs du CERN,” .
- [35] “LHC public plots,” [ATLAS Twiki](#).
- [36] G. Aad *et al.* (ATLAS), *JINST* **3**, S08003 (2008).

- [37] The ATLAS collaboration, *ATLAS magnet system: Technical Design Report* (1997).
- [38] The ATLAS collaboration, *ATLAS liquid argon calorimeter: Technical Design Report* (1996).
- [39] The ATLAS collaboration, *ATLAS muon spectrometer : Technical Design Report* (1997).
- [40] The ATLAS collaboration, *ATLAS high-level trigger, data acquisition and controls: Technical Design Report* (2003).
- [41] “LHC upgrades and operation,” CERN Website.
- [42] *Technical Design Report for the Phase-II Upgrade of the ATLAS Muon Spectrometer*, Tech. Rep. CERN-LHCC-2017-017. ATLAS-TDR-026 (CERN, Geneva, 2017).
- [43] T. Kawamoto, S. Vlachos, L. Pontecorvo, J. Dubbert, G. Mikenberg, P. Iengo, C. Dallapiccola, C. Amelung, L. Levinson, R. Richter, and D. Lellouch, *New Small Wheel Technical Design Report*, Tech. Rep. CERN-LHCC-2013-006. ATLAS-TDR-020 (2013) aTLAS New Small Wheel Technical Design Report.
- [44] G. Aielli, C. Amelung, D. Boscherini, R. Cardarelli, M. Corradi, L. Han, V. Izzo, O. Kortner, H. Kroha, D. Levin, L. Massa, L. Paolozzi, R. Santonico, and R. Vari (ATLAS Collaboration), *The ATLAS BIS78 Project*, Tech. Rep. ATL-MUON-INT-2016-002 (CERN, Geneva, 2016).
- [45] ATLAS Collaboration (ATLAS), *muTrigNt\_write code*, Tech. Rep.
- [46] ATLAS Collaboration (ATLAS), *Muon Upgrade Studies Twiki*, Tech. Rep.
- [47] L.Marcoccia, *Phase II Upgrade : High-eta tagger + RPC (Muon Week)*, Tech. Rep. (2018).
- [48] L. Marcoccia, *Efficiency studies on emulated RPC for the Phase-II Upgrade of the ATLAS Muon Spectrometer*, Tech. Rep. ATL-COM-MUON-2019-060 (CERN, Geneva, 2019).